

A GLOBAL NUCLEON OPTICAL MODEL POTENTIAL*

R.L. VARNER

*Oak Ridge National Laboratory, Oak Ridge, TN 37831-6368, USA
and Triangle Universities Nuclear Laboratory, Duke University, Durham, NC 27706, USA*

and

W.J. THOMPSON, T.L. McABEE**, E.J. LUDWIG and T.B. CLEGG

*Department of Physics and Astronomy, University of North Carolina, Chapel Hill, NC 27599-3255, USA
and Triangle Universities Nuclear Laboratory, Duke University, Durham, NC 27706, USA*

Editor G.E. Brown

Received July 1990

Contents:

1. Introduction	59	4. Optical-model analysis procedures	90
1.1. Motivations for global optical-model potentials	59	4.1. The optical-potential search program MINOPT	91
1.2. Features of the CH89 global potential	60	4.2. Studies using synthetic data	93
1.3. Previous extensive optical-model analyses	61	4.3. Best-fit estimators	94
1.4. Motivation for this analysis	62	4.4. Search procedures	96
1.5. Outline of the report	66	5. Estimating optical-model parameter uncertainties	97
2. Parametrizing the optical potential	67	5.1. Relevant statistics and probability theory	98
2.1. Folding-model guidelines	67	5.2. The bootstrap uncertainty analysis	101
2.2. Form of the optical potential	68	5.3. A simple example of the bootstrap	101
2.3. Real central potential	70	5.4. Bootstrapping for optical-potential uncertainties	103
2.4. Coulomb potential and Coulomb correction	71	6. The global optical potential, conclusions and outlook	106
2.5. Spin-orbit potential	73	6.1. The optical-model potential CH89	106
2.6. Absorptive central potential	73	6.2. Parameter uncertainties, correlations and their uses	110
3. Database of nucleon elastic scattering	75	6.3. Comparison with previous global analyses	114
3.1. Database criteria	75	6.4. Outlook	115
3.2. Polarized proton data from TUNL	78	References	117
3.3. Other data for the database	83		

* Research sponsored in part by the Division of Nuclear Physics, US Department of Energy under grant DE-FG05-88ER40442 to the University of North Carolina and contract DE-AC05-84OR21400 with Martin Marietta Energy Systems, Inc.

** Present address: Lawrence Livermore National Laboratory, Livermore, CA 94550, USA.

Single orders for this issue

PHYSICS REPORTS (Review Section of Physics Letters) 201, No. 2 (1991) 57–119.

Copies of this issue may be obtained at the price given below. All orders should be sent directly to the Publisher. Orders must be accompanied by check.

Single issue price Dfl. 48.00, postage included.

A GLOBAL NUCLEON OPTICAL MODEL POTENTIAL

R.L. VARNER

*Oak Ridge National Laboratory, Oak Ridge, TN 37831-6368, USA
and Triangle Universities Nuclear Laboratory, Duke University, Durham, NC 27706, USA*

and

W.J. THOMPSON, T.L. McABEE, E.J. LUDWIG and T.B. CLEGG

*Department of Physics and Astronomy, University of North Carolina, Chapel Hill,
NC 27599-3255, USA
and Triangle Universities Nuclear Laboratory, Duke University, Durham, NC 27706, USA*



NORTH-HOLLAND

Abstract:

We describe a new parametrization of the nucleon–nucleus optical-model potential based on data for $A = 40$ to 209, proton energies of 16 to 65 MeV and neutron energies of 10 to 26 MeV, including extensive polarized-beam data. This parametrization, called CH89, is based on the current understanding of the basis of the optical potential, such as the folding model and nuclear matter approaches. It differs significantly from previous global parametrizations, especially in the weakness of the isovector potential, the parametrization of potential radii, and the smooth variation of imaginary-potential depths with energy. We also describe an optical-model parameter search system, MINOPT, based on the minimization program MINUIT. It is applied to analyze simultaneously a large database of nearly 300 carefully selected angular distributions. Parameter uncertainties and correlations between parameters are estimated by using the non-parametric statistical technique known as the bootstrap method. CH89 is intended to serve as a starting point for definitive tests of models of the nucleon–nucleus interaction, and to be of immediate use for applications.

1. Introduction

We report a new parametrization of the nucleon–nucleus optical-model potential appropriate to the target-nucleus mass range $A = 40$ –209 and the nucleon laboratory energy range $E = 10$ –65 MeV. The parametrization, which we designate as CH89, is based on an extensive database of accurately measured cross-section and analyzing-power angular distributions, and it involves large-scale searches using proven strategies for this type of data. Particular attention is given to estimating parameter uncertainties and correlations between parameters.

Our research makes use of an improved understanding of the physics of the optical potential, including the many-nucleon problem and the folding-model approximation, which has been obtained since the pioneering analysis of Becchetti and Greenlees [1] two decades ago. The form of our parametrization is derived from considerations of the nucleon optical potential in nuclear matter [2, 3], on the folding-model potential for finite nuclei, and on previous phenomenology. We provide several results (summarized in section 1.2) that are significantly different from the results of the analysis of Becchetti and Greenlees, and which should lead to new insight into the nuclear many-body problem, as well as being immediately applicable.

The emphasis in this report is on a reliable estimation of the optical-model potential, on uncertainties in the parameters of the potential, and on relations (correlations) between its parameters, rather than on extensive interpretation of the resulting potentials. We decided that, apart from pointing out features of the new parametrization, the task of interpreting such a reliably determined potential is much too extensive to be included here. The spirit of our analysis is therefore similar to that of the recent meson-exchange model of the nucleon–nucleon interaction, the Bonn potential [4], but with less theoretical underpinning because of the more complicated nature of nucleon–nucleus scattering. Because we have obtained, for the first time, reliable estimates of the correlations between global parameters, we also describe, with a pedagogical emphasis, how the correlation coefficients may be interpreted and used.

1.1. Motivations for global optical-model potentials

The nucleon–nucleus optical model is the reduction of the complicated many-body problem of the scattering of a nucleon from a nucleus to the scattering of a single particle from a complex one-body potential. The existence of such a potential was formally shown by Feshbach [5], and the theory and phenomenology have been extensively reviewed by Hodgson [6], Satchler [7] and Rapaport [8], and in recent conferences such as that given in ref. [9].

A global nucleon–nucleus optical-model potential has parameters that are smooth functions of target A and Z , projectile type (proton or neutron), and laboratory bombarding energy (E) and it describes

data over a wide range of these variables. Such parameters are in some way averages over values that best describe nucleon elastic scattering over limited ranges of A , Z , and E . Our analysis describes (p, p) and (n, n) scattering from target nuclei in the valley of stability with $40 \leq A \leq 209$ and $10 \leq E \leq 65$ MeV.

Experimentally based global optical-model potentials have broad applications in nuclear science. At a fundamental level they can be used to test microscopically calculated potentials such as those based on the nuclear-matter approach [2], and to infer the density dependence of the underlying effective interaction from their density dependence [10]. At a more practical level, global optical potentials can be used to predict nucleon–nucleus potentials if elastic scattering data cannot be obtained, as for nuclei far from the valley of stability. Such data are required for modeling r -process nucleosynthesis in nuclear astrophysics [11] and in fusion reactor engineering design [12].

In an earlier report [13] we summarized the parameter values obtained in a global analysis. We refer to that parametrization as CH86 (Chapel Hill 1986). The parameter set that we report here, called CH89, is nearly the same as CH86, but it is shown in section 6.1 to be more significant because the uncertainty analysis (section 5) shows that the parameters are more precise than we believed when CH86 was derived. As promised in our brief report [13], we provide here the details of our analysis. All the data and a preliminary version of the analysis are described in ref. [14].

1.2. Features of the CH89 global potential

The features of our global potential that distinguish it from the previously most extensive analysis, that of Becchetti and Greenlees [1], are the following:

(i) The quality of fit to our database of nearly 300 angular distributions (9000 data points) of proton and neutron differential cross sections and analyzing powers, as indicated by a least-squares fit, is three times better than obtained with the Becchetti–Greenlees potential, which uses nearly the same number of parameters (16) as in our analysis (20). For the first time in a large-scale analysis, we provide the parameter uncertainties and the correlation coefficients between parameters which are necessary for meaningful interpretation or use of the parameters.

(ii) The real potential has an isovector strength, $V_t = 13 \pm 1$ MeV, which is about half that commonly used. This much weaker isospin dependence has important consequences for extrapolating the optical potential to unstable nuclei. The smaller, reliable, value that we obtain is a consequence of simultaneously analyzing proton and neutron data, whereas ref. [1] analyzed the neutron and proton data separately.

(iii) The radius parameters of the real nuclear, Coulomb, imaginary and spin–orbit potentials each require an offset term in addition to the usual $A^{1/3}$ proportionality of potential radii. Such offset terms are well known [15] from parametrizations of nuclear charge radii, $R_c = r_c A^{1/3} + r_c^{(0)}$, in which $r_c^{(0)}$ is an offset radius. Similar offset radii are therefore predicted in folding models of the nucleon–nucleus potential, as we show in section 2.1 and have been observed in at least one previous global analysis [23]. It is necessary to include the correct A -dependence in the potential radii to avoid introducing non-isospin effects into the isospin-dependent terms of the depths, since $\varepsilon = (N - Z)/A$ is nearly proportional to A along the line of isotopic stability [16].

(iv) In CH89 the depths of the imaginary potential vary smoothly with energy, so that there is a smooth transition from low-energy surface absorption to high-energy volume absorption. The CH89 absorptive potential is therefore more realistic than in previous analyses [1, 8], and it also satisfies empirical observations that the absorptive volume integral (section 1.4.3) is essentially constant over the range $10 < E < 150$ MeV [17, 18]. The price we pay for such improvements is that the absorptive

potential below 10 MeV probably does not behave as a simple extrapolation of the energy dependence found here. This energy restriction also limits the usefulness of CH89 in studies of dispersion-relation constraints on the relation between real and imaginary potentials [19].

(v) We find that the spin-orbit depth is independent of E and A for $10 < E < 65$ MeV and $40 < A < 209$. It is isospin independent and there is no need for an imaginary component.

The optical model we describe here is based on Woods–Saxon form factors, well known in nucleon optical-model potentials. This choice is sensible, since we are attempting to parametrize data from a wide range of A and E , over which detailed variations in the form factors (as might be observed in detailed Fourier–Bessel analyses [20]) are averaged. We constrained data to the mass range $A \geq 40$. This avoids well-known difficulties for $A < 40$ in finding an optical potential that varies smoothly with E , because of the low density of scattering states in light nuclei. We also constrained the data to the energy range $10 \leq E \leq 65$ MeV to avoid problems with compound elastic scattering at lower energies and with relativity at higher energies.

We use an optical potential in a non-relativistic Schrödinger equation, in spite of significant advances in understanding Dirac-based relativistic approaches [21]. The non-relativistic wave equation is chosen for three reasons. First, the data we analyze are in an energy range (10 to 65 MeV) where relativistic effects, at least in the kinematics, are probably small. At the maximum incident energy of 65 MeV the incident momentum has a relativistic correction of less than 2%. Second, part of our goal is to provide, for this energy range, a potential useful in nuclear physics calculations, which are usually made with the Schrödinger equation. Third, the microscopically derived potentials with which CH89 may be compared [3] are non-relativistic.

1.3. Previous extensive optical-model analyses

Although several previous extensive optical-model analyses of nucleon–nucleus scattering for $E \leq 65$ MeV have been made, the present analysis is sufficiently different and improved that a comparison is worthwhile.

The Becchetti and Greenlees global parametrization as a function of N , Z , and E [1] is the most widely used, but it is now two decades old. Their database consisted of about 2500 proton and 1000 neutron data for targets of $A \geq 40$ (dominated by data for $A \leq 90$) and $E \leq 40$ MeV, including some reaction, total cross-section, and polarization data. They performed separate analyses of (p, p) and (n, n) data, using the best proton potential as the starting point for the neutron analysis. They tested several different parametrizations of the optical potential, and they used an automated fitting program. Their final parametrization included linear energy dependences for all the central depths, and a simple dependence of the depths on the isospin asymmetry, ε . The potential radii were assumed to be proportional to $A^{1/3}$, and they used a simple model for the real, central-potential Coulomb correction [22]. For comparison, we list their parameters in table 1.

The neutron cross-section analyses by Rapaport et al. [8, 23] used a database of about 500 points for $A = 40, 90, 92, 116, 124, 208$, with $11 \leq E \leq 26$ MeV, all measured at Ohio University. They explored the asymmetry dependence of the potentials and parametrizations of the real radius differing from the usual $A^{1/3}$ proportionality. The spin-orbit potential was fixed during the search at Becchetti–Greenlees values. The resulting best-fit potential [8] is given in table 2. We included their data in our database.

There have been other, smaller-scale analyses of nucleon–nucleus scattering for a range of values of A and E . Patterson et al. [24] used 12 angular distributions of (p, n) and (n, n) cross-section data in a Lane-model analysis to estimate the isovector parts of the optical potential. They found the isovector

Table 1
Becchetti–Greenlees [1] parameters for proton and neutron scattering, in the notation of CH89, described in section 2.2

(p, p)	$V = 54.0 - 0.32E + 0.4Z/A^{1/3} + 24.0\epsilon \text{ MeV},$ $R_0 = 1.17A^{1/3} \text{ fm}, \quad a_0 = 0.75 \text{ fm},$ $V_{so} = 6.2 \text{ MeV fm}^2, \quad R_{so} = 1.01A^{1/3} \text{ fm}, \quad a_{so} = 0.75 \text{ fm},$ $W_v = -2.7 + 0.22E \text{ MeV}, \quad W_v > 0,$ $W_s = 11.8 - 0.25E + 12.0\epsilon \text{ MeV}, \quad W_s > 0,$ $R_w = 1.32A^{1/3} \text{ fm}, \quad a_w = 0.51 + 0.7\epsilon \text{ fm}.$
(n, n)	$V = 56.3 - 0.32E - 24.0\epsilon \text{ MeV},$ $R_0 = 1.17A^{1/3} \text{ fm}, \quad a_0 = 0.75 \text{ fm},$ $V_{so} = 6.2 \text{ MeV fm}^2, \quad R_{so} = 1.01A^{1/3} \text{ fm}, \quad a_{so} = 0.75 \text{ fm},$ $W_v = -1.56 + 0.22E \text{ MeV}, \quad W_v > 0,$ $W_s = 13.0 - 0.25E - 12.0\epsilon \text{ MeV}, \quad W_s > 0,$ $R_w = 1.26A^{1/3} \text{ fm}, \quad a_w = 0.58 \text{ fm}.$

Table 2
Rapaport, Kulkarni and Finlay [8, 23] neutron global optical-model potential, global potential A , using the notation of CH89, described in section 2.2

$V = 54.19 - 0.33E - (22.7 - 0.19E)\epsilon \text{ MeV},$ $R_0 = 1.198A^{1/3} \text{ fm}, \quad a_0 = 0.663 \text{ fm},$ $V_{so} = 6.2 \text{ MeV fm}^2, \quad R_{so} = 1.01A^{1/3} \text{ fm}, \quad a_{so} = 0.75 \text{ fm},$ $W_v = 0.0 \text{ MeV},$ $W_s = 4.28 + 0.4E - 12.8\epsilon \text{ MeV},$ $W_a = -3.95 + 0.37E \text{ MeV},$ $W_d = 13.5 - 0.35E - 9.3\epsilon \text{ MeV},$ $R_w = 1.295A^{1/3} \text{ fm}, \quad a_w = 0.59 \text{ fm}.$	$\left. \begin{array}{l} E \leq 15 \text{ MeV}, \\ E \geq 15 \text{ MeV}, \end{array} \right\}$
---	---

(asymmetry) potential to be significantly smaller than in previous analyses such as Becchetti–Greenlees, and they were able to describe the (p, n) and (n, n) cross-section data well.

At higher energies, $60 \leq E \leq 200 \text{ MeV}$, systematic elastic scattering data with polarized beams are now available; the analysis by Nadasen et al. [18] used (p, p) scattering from ^{40}Ca , ^{90}Zr , and ^{208}Pb , in an analysis containing about 1500 data points. They corrected for relativistic effects by using an approximate reduction of the Dirac equation to the Schrödinger equation and relativistic kinematics for the projectile. They deduced a logarithmic energy dependence for the real central-potential depth and a volume absorption potential relatively constant up to $E = 140 \text{ MeV}$.

1.4. Motivation for this analysis

Our analysis was motivated by three major advances in nuclear physics in the twenty years since the work of Becchetti and Greenlees [1]: (i) a better understanding of the theoretical basis of the optical model, (ii) greater accuracy and completeness of data for cross sections, $\sigma(\theta)$, and vector analyzing powers, $A_y(\theta)$, and (iii) an improved ability to optimize many parameters reliably in searches on large databases. With this motivation, we employed a semiempirical approach to the optical-model potential, in which we selected theoretically reasonable N , Z , and E dependences for the parameters, then used these to parametrize reliably a wide range of nucleon elastic-scattering data. We now describe each of these advances in more detail.

1.4.1. Current understanding of the optical potential

The analyses described in section 1.3 were similar in that they used form factor radii simply proportional to $A^{1/3}$, diffuseness parameters and spin-orbit depths independent of A and E , mixtures of surface and volume components in the form factor of the imaginary potential, and well depths linearly dependent on E .

However, there is now sufficient understanding of microscopic models [25] to predict a global parametrizations. For real central and spin-orbit potentials, we describe in section 2.1 folding-model potentials using realistic nuclear densities and effective interactions to suggest parametrizations. For the absorptive potential, the phenomenology of its volume integrals and some microscopic predictions suggest parametrizations of its E - and A -dependences, as discussed in section 2.6.

The folding model. The optical potential can be estimated from a semi-microscopic basis, usually by means of the folding model, first applied extensively to nucleon elastic scattering by Greenlees et al. [26]. In this model the potential is calculated as the superposition of interactions between an incident nucleon and each target nucleon, in the approximation that the incident nucleon does not perturb the target density distribution. In the folding model, the central potential (for example) is [7, p. 475]

$$V_{\text{FM}}(r) = \int v(|r - r'|) \rho(r') dr', \quad (1.1)$$

in which $v(|r - r'|)$ is an effective nucleon-nucleon potential and $\rho(r')$ is the point density distribution of target nucleons, inferred from the charge distribution measured by (e, e) scattering or calculated from a self-consistent model of the target ground state [27]. For the folding model of the spin-orbit potential, similar (but more involved) formulas are obtained [28].

Folding-model integrals. One general result from the folding model in the form of eq. (1.1) is that V_{FM} may be characterized by its volume integrals and mean-square radii (MSR) [26], independent of the details of the density distributions. The volume integrals of the central potentials, $V(r)$, are defined by

$$J \equiv 4\pi \int V(r) r^2 dr. \quad (1.2)$$

The significance of the volume integrals is that in the folding model, for density-independent effective interactions, they reduce to the volume integral of the effective nucleon-nucleon interaction, v , multiplied by the A -value of the target [7, app. C],

$$J = A \int v(s) s^2 ds, \quad (1.3)$$

where s is the nucleon-nucleon separation. Thus, for a folding-model potential, J/A characterizes the underlying effective interaction independently of the nuclear density distribution.

The mean-square radius (MSR) of a scattering potential is defined by

$$\langle r^2 \rangle_{\text{pot}} \equiv \int r^2 V(r) r^2 dr / \int V(r) r^2 dr. \quad (1.4)$$

If $V(r)$ results from folding a density distribution with a finite-range, density-independent interaction, then

$$\langle r^2 \rangle_{\text{pot}} = \langle r^2 \rangle_{\rho} + \langle r^2 \rangle_v, \quad (1.5)$$

where $\langle r^2 \rangle_{\rho}$ is the MSR of the density distribution and $\langle r^2 \rangle_v$ is the MSR of the effective interaction. For density-dependent effective interactions the formulas are modified [10, 29]. Because of the expected simple behavior of the volume integral and MSR, they are often used to compare and characterize the potentials.

For the spin-orbit potential a slightly different integral, J_2 , gives the integral of the effective nucleon-nucleon interaction independent of the density distribution,

$$J_2 = 4\pi \int r^2 V_{\text{so}}(r) r^2 dr, \quad (1.6)$$

for which the MSR is

$$\langle r^2 \rangle_2 = \frac{4\pi}{J_2} \int r^4 V_{\text{so}}(r) r^2 dr. \quad (1.7)$$

Phenomenological properties of volume integrals. In determining phenomenological properties of optical potentials it is found that parameters derived from fits to individual nuclei at single energies vary considerably from nucleus to nucleus and with energy [16], which makes the extraction of global potential properties from individual fits difficult. Therefore, global properties of optical potentials are usually summarized in terms of volume-integral and MSR values. However, information on potential depths (which is important for nuclear matter) and on potential geometries (relevant to nuclear structure) is thereby lost.

The observed properties of empirically determined volume integrals are summarized in several references [6–8]. The most noteworthy properties are: (i) J/A for the real central potential decreases almost linearly with increasing E for $10 \leq E \leq 80$ MeV [3]; (ii) J/A of the real central potential is approximately constant with A for proton scattering [30], but it decreases with A for neutron potentials [8]; (iii) J/A for the absorptive potential is almost constant with A and E in the proton potentials [17], but decreases with target A in the neutron potentials [8]; (iv) for the spin-orbit potential J_2/A varies slowly with A and E [31, 32].

Most of these volume-integral properties are well determined for proton scattering. Results for neutron scattering, summarized in ref. [8], are less definitive. One goal of our analysis was to have a better balance between (p, p) and (n, n) data to remedy this defect.

1.4.2. Availability of nucleon elastic scattering data

After deciding on a form for the potential and the parameters to be used, selection of the database of elastic scattering data has the greatest influence on the resulting parametrization. Many data used by Becchetti and Greenlees [1] were extracted from the literature, and those in other analyses mentioned in section 1.3 were generally limited to a few target nuclei. Previous proton data were principally unpolarized elastic-scattering $\sigma(\theta)$ measurements and limited absorption cross-section measurements, supplemented by a few polarization data measured by double scattering. The small number of

polarization data and the severe systematic uncertainties affecting them, compared with the accurate $A_y(\theta)$ data that are now available, limited the reliability of the parametrization of the spin-orbit and absorptive potentials.

Previous neutron data were almost entirely cross sections, differential elastic-scattering or total, many measured at energies below 10 MeV where significant compound-elastic-scattering corrections are required. There were also many fewer neutron data sets than proton data sets. This was unfortunate, since the greatest sensitivity of elastic scattering to the isovector potential occurs in the comparison of neutron and proton scattering from the same, or nearby, nuclei [16], as we discuss in section 4. An additional difficulty with previous analyses was that data for various targets and energies were measured at many different laboratories. Different, usually unstated, systematic errors, such as in the normalization of $\sigma(\theta)$, can cause effects that can be mistaken for E - or A -dependences [22].

The database for the CH89 potential (detailed in section 3) is improved over those used previously in the following way.

(i) Systematic measurements from laboratories emphasizing elastic scattering studies have been used. These measurements on large numbers of targets used the same scattering apparatus and techniques, thus rendering systematic errors similar among groups of targets, and therefore more readily discernible and correctable.

(ii) By using polarized ion sources for protons and efficient polarization transfer reactions for neutron production, one can measure easily (and simultaneously for protons) accurate A_y and σ data. Analyses of such data provide strong constraints on the spin-orbit and absorptive potentials. Unlike double-scattering polarization measurements, systematic errors in $A_y(\theta)$ can be made negligibly small.

(iii) The energy range of our neutron database is now such (10 to 26 MeV) that only data for $E \geq 10$ MeV need be used, reducing the effect of compound-elastic scattering, especially with the restriction made in our analysis to $A \geq 40$.

(iv) Precise neutron A_y data are now available [33], enabling us to analyze neutron data on a similar footing to proton data.

1.4.3. Parameter optimization procedures

There are two distinct ways to estimate global optical model parameters from the data. One is to fit each data set of $\sigma(\theta)$ and $A_y(\theta)$ separately, adjusting parameters to achieve the best fit. As pointed out in section 1.2, this often produces parameters that fluctuate with A and E . A smoothing procedure often adopted is to average the geometric parameters with respect to A and E , then repeat individual fitting using this fixed geometry. The resulting depths are then fitted to functions of A , E , and isospin, to give a broader parametrization [23], which is then slightly adjusted to fit the data optimally. This technique has often been chosen because individual fits were available from other work, and because the strong parameter correlations in the optical model tend to confuse many search algorithms. Although practical for a small database, the technique is impractical for an extensive analysis with a large database.

The second approach to a global parametrization is to postulate a global model as a function of N , Z , E and nucleon type (p or n), then to vary the model parameters to optimize the fit to all the data simultaneously [1]. This technique is the better approach for analyzing large databases. Its success needs two technologies; a search technique that is stable and efficient even when searching on 10 to 15 correlated parameters, and the existence of fast computers.

It is also desirable to report confidence intervals and parameter correlations for a meaningful interpretation of the resulting parametrization. For example, to compute the uncertainty in functions of

optical model parameters, such as volume integrals, requires knowing parameter correlations [35]. Parameter uncertainties and correlations have not been reliably obtained in previous analyses, but are described here in sections 5 and 6.2.

Raw computing power is also needed for global fitting. Although there are search algorithms, such as embodied in the program MINUIT [34], which are capable of stable searches on dozens of parameters, they may require thousands of calculations to examine properly the parameter space. The use of fast, scalar processors running at 2 MFLOPS (million floating point operations per second), available in modern scientific work stations, allowed us to execute in about 1 h a search on a 20-parameter optical potential using 150 data sets (9000 data points). Details of these computations are given in sections 4 and 5.

During our analysis we determined that many of the uncertainty and correlation estimates given by the optimization program MINUIT are unreliable in our application. Therefore we used the novel bootstrap statistical method to make more reliable estimates, as described in section 5. This reliability was obtained at the expense of much more computer time, 50 h per estimate.

1.5. Outline of the report

In the following five sections we detail the procedures we used to obtain the CH89 parametrization of the nucleon–nucleus optical potential. In section 2 we describe how we used the folding model to suggest the form of the real parts of the optical potential, and the phenomenology of the absorptive

Table 3

Global optical-model parametrization for CH86 and CH89. The values a_0 , a_w , V_{so} , and a_{so} are independent of A , Z , and $E = E_{\text{lab}}(\text{MeV})$

Real central potential:

$$V_r = V_0 \pm V_t \frac{N-Z}{A} + (E - E_c)V_c, \quad +: \text{ protons, } -: \text{ neutrons,}$$

$$R_0 = r_0 A^{1/3} + r_0^{(0)},$$

$$E_c = \begin{cases} \frac{6Ze^2}{5R_c} = \frac{1.73Z}{R_c} \text{ MeV,} & \text{for (p, p),} \\ 0, & \text{for (n, n).} \end{cases}$$

Coulomb potential radius:

$$R_c = r_c A^{1/3} + r_c^{(0)} = 1.238 A^{1/3} + 0.116 \text{ fm.}$$

Spin-orbit potential:

$$R_{so} = r_{so} A^{1/3} + r_{so}^{(0)}.$$

Imaginary central potential:

$$W_v = W_{v0} \left[1 + \exp\left(\frac{W_{ve0} - (E - E_c)}{W_{vew}}\right) \right]^{-1},$$

$$W_s = \left(W_{s0} \pm W_{st} \frac{N-Z}{A} \right) \left[1 + \exp\left(\frac{(E - E_c) - W_{se0}}{W_{sew}}\right) \right]^{-1},$$

$$R_w = r_w A^{1/3} + r_w^{(0)}.$$

potential to suggest appropriate forms for it as a function of N , Z , and E . Assembly of the 9000 point database of accurate proton and neutron elastic-scattering σ and A_y is described in section 3.

In section 4 we describe our optical-model analysis procedures, including the search program developed, studies using synthetic data, criteria for best-fit estimators, and the final search procedures. Since a key feature of the usefulness of CH89 is a reliable estimation of the parameter uncertainties and of correlations between parameters, we provide in section 5 a summary of the relevant statistics and probability theory as a background to the bootstrap uncertainty analysis we developed; then we show how it was applied for the optical-model analysis. Finally, in section 6 we present our results and conclusions, comparisons with previous results, and possibilities for future research in this area.

To those for whom the journey is less interesting than the destination, we give the form of the CH89 potential in eqs. (2.3), (2.4) and in table 3; the parameter values with uncertainties in table 6, and the correlation coefficients between parameters in table 7.

2. Parametrizing the optical potential

In this section we describe how we decided on the form of the optical-model potential used in our global analysis. There are two levels of parametrization: (i) For each (N, Z) and projectile (p or n) at given laboratory energy E , one must parametrize the geometry of the potential, its central real and imaginary parts, and the spin-orbit interaction. (ii) For the whole database one must decide how the geometric parameters and the potential depths are to vary with N , Z , E , and nucleon type (p or n).

For CH89 we used the folding model (sections 1.4.1 and 2.1) primarily to establish plausible forms for the A -dependence of the geometry, and we used microscopic calculations of the optical potential, especially the nuclear-matter approach [2, 3], to suggest the N -, Z -, and E -dependences of the potential depths. We summarize these considerations in the following subsections.

2.1. Folding-model guidelines

Following the discussion in sections 1.4.1, we use nuclear ground-state densities and realistic effective interactions to model the real parts of the potential for nucleon-nucleus scattering, with particular emphasis on the geometric parameters. We summarize relevant aspects of our folding-model calculations. More detail is given elsewhere [36].

We used accurately determined two-parameter Fermi (2pF) charge densities [36–38] for electron scattering from nuclei in the mass range $40 \leq A \leq 209$ (the range of our optical-model analysis) and parametrized the charge radii in a least-squares fit. We then derived the geometric parameters of the nuclear charge densities as a function of nuclear mass, A , namely the charge radius

$$R_{\text{cd}}(A) = 1.238A^{1/3} - 0.72 \text{ fm} \quad (2.1)$$

and charge diffuseness $a_{\text{cd}} = 0.56 \text{ fm}$. We note immediately that charge radii have an offset term, here -0.72 fm , and that such radius offsets eventually appear in the nucleon-nucleus potential. From the charge densities we also derived [36] point-proton densities by unfolding the proton and neutron internal distributions. We then assumed that the neutron and proton densities are the same, so that the matter and point-proton densities coincided. Such an approximation is sufficiently reliable for our

purposes, and leads to the usual $(N - Z)/A$ dependence of the real-well depths. The matter radius derived was,

$$R_M = 1.25 A^{1/3} - 0.71 \text{ fm} \quad (2.2)$$

and the matter diffuseness was $a_M = 0.51 \text{ fm}$.

The effective interaction used in the folding model has the same spin and isospin structure as the free nucleon–nucleon interaction [7, p. 638]. It differs from the free interaction because of effects from the surrounding nucleons, such as exchange (Pauli blocking). One can estimate the effective interaction by varying its parameters in a folding-model calculation of the optical potential to fit the elastic scattering data [26, 39]. This is successful, but very computationally intensive, and so it not well suited to a large-scale analysis, although it has the advantage that the radial form is not constrained to simple analytic forms.

For the effective interaction in eq. (1.1) we used the potential M3Y [40] and some variants of it. Pauli blocking effects were estimated by using a local Slater exchange approximation. The folding integrals were evaluated numerically. The calculated potentials were fitted with 2pF functions, and yielded potentials with the same $A^{1/3}$ coefficient as in eq. (2.2), a larger offset radius, and a somewhat larger diffuseness, because of the finite range of the effective interaction. Similar, but more elaborate calculations were made for the folding-model spin–orbit potential, following ref. [28].

2.2. Form of the optical potential

Our folding-model calculations described in section 2.1 were adequately parametrized by 2pF functions in the surface region. Our analyses are most sensitive to the surface region, because of relatively strong nucleon absorption. Therefore, we used 2pF functions for the radial form factors of the nuclear part of the potential, but call them Woods–Saxon (WS) form factors, in accord with usual practice. There has been much recent work on alternatives to WS form factors, especially using Fourier–Bessel expansions [20] to represent deviations from the basic WS function. These variations are usually in the details of the quality of fits and of the potential in the nuclear interior. With current computational limitations, the effort is not justified for such a global analysis. We write for the WS form factor

$$f_{ws}(r, R, a) = \frac{1}{1 + \exp[(r - R)/a]} \quad (2.3)$$

For components of the optical potential that are surface peaked we use form factors that are radial derivatives of WS form factors.

We write the local optical potential for nucleon–nucleus scattering as

$$V(r) = -V_r f_{ws}(r, R_0, a_0) - iW_v f_{ws}(r, R_w, a_w) - iW_s(-4a_w) \frac{d}{dr} f_{ws}(r, R_w, a_w) \\ - 2(V_{so} + iW_{so}) \left(\frac{-1}{r} \frac{d}{dr} f_{ws}(r, R_{so}, a_{so}) \mathbf{l} \cdot \boldsymbol{\sigma} \right)$$

$$\begin{aligned}
 & + \begin{cases} \frac{Ze^2}{r}, & r \geq R_c \\ \frac{Ze^2}{2R_c} \left(3 - \frac{r^2}{R_c^2}\right), & r \leq R_c \end{cases} \quad \text{for incident protons,} \\
 & + 0 \quad \text{for incident neutrons.} \quad (2.4)
 \end{aligned}$$

For future reference we record the volume integrals, J_i , $i = R, w$, and the mean-square radii (MSR), $\langle r_i^2 \rangle$, $i = R, w$, which were introduced in section 1.4.1. For the components of the potential in eq. (2.4) these are

$$\frac{J_R}{A} = \frac{J_0(V_0, R_0, a_0)}{A} = \frac{4\pi}{3} \frac{R_0^3}{A} V_0 \left[1 + \left(\frac{\pi a_0}{R_0} \right)^2 \right], \quad (2.5)$$

$$\langle r^2 \rangle_R = \frac{3}{5} R_0^2 \left[1 + \frac{7}{3} \left(\frac{\pi a_0}{R_0} \right)^2 \right] \quad (2.6)$$

for the real part of the central potential, while

$$\begin{aligned}
 \frac{J_w}{A} &= \frac{J_0(W_v, R_w, a_w)}{A} + \frac{J_0(W_s, R_w, a_w)}{A} \\
 &= \frac{4\pi}{3} \frac{R_w^3}{A} \left\{ W_v \left[1 + \left(\frac{\pi a_w}{R_w} \right)^2 \right] + \frac{12a_w}{R_w} W_s \left[1 + \frac{1}{3} \left(\frac{\pi a_w}{R_w} \right)^2 \right] \right\}, \quad (2.7)
 \end{aligned}$$

$$\begin{aligned}
 \langle r^2 \rangle_w &= J_w^{-1} [\langle r^2 \rangle_{wv} J_{wv} + \langle r^2 \rangle_{ws} J_{ws}] \\
 &= \frac{1}{J_w} R_w^2 \left\{ \frac{3}{5} J_{wv} \left[1 + \frac{7}{3} \left(\frac{\pi a_w}{R_w} \right)^2 \right] + J_{ws} \left[1 + \frac{5}{3} \left(\frac{\pi a_w}{R_w} \right)^2 \right] \right\} \quad (2.8)
 \end{aligned}$$

for the imaginary part of the central potential.

For the spin-orbit potential the corresponding integrals that can be related to the folding model (section 2.1) are [see eq. (1.6)]

$$\frac{J_{so}}{A} = \frac{J_2(V_{so}, R_{so}, a_{so})}{A} = 8\pi \frac{R_{so}^3}{A} V_{so} \left[1 + \left(\frac{\pi a_{so}}{R_{so}} \right)^2 \right], \quad (2.9)$$

$$\langle r^2 \rangle_{so} = R_{so}^2 \left[1 + \frac{7}{3} \left(\frac{\pi a_{so}}{R_{so}} \right)^2 \right]. \quad (2.10)$$

Note that eqs. (2.5) through (2.10) are leptodermous expansions in powers of the ratio of diffuseness to radius [41], they are accurate to 0.01% for the geometric parameters obtained here.

Although the folding model discussed in sections 1.4.1 and 2.1 is useful for guiding the choice of potential geometry, it is not adequate to predict the potential strength dependence on energy and isospin. It is also quite inadequate for describing imaginary parts of the potential, because it is constructed only from ground-state densities and ignores reaction processes. In what follows we describe and justify our choices for the N -, Z -, and E -dependences of the parameters in eq. (2.4).

2.3. Real central potential

For the real central potential, we expect that the folding-model predictions, which use simple effective interactions, are not correct for the real central-potential depth, V_r , even if the exchange effects are appropriately included, since additional poorly understood energy and density dependence in the effective interaction are expected [10]. Since we lack guidance from the folding model for V_r , we use phenomenology [16] as a guide and parametrize the depth as

$$V_r = V_0 + V_c(E - E_c) \pm [V_t - V_{te}(E - E_c)]\varepsilon, \quad (2.11)$$

where the isospin asymmetry, $\varepsilon = (N - Z)/A$, and the “+” sign is for (p, p) scattering and the “-” sign is for (n, n) scattering. The linear energy dependence of V_r is consistent with previous analyses in the range $10 \leq E \leq 65$ MeV [16].

The isovector term in eq. (2.11) reflects differences between neutron–nucleus and proton–nucleus scattering that arise from the hadronic part of the interaction. It results predominantly from the Pauli principle in nuclei [6, 42]. The principal difficulty in determining the isovector potential is that it contributes only about 4% of the total potential for $40 \leq A \leq 209$ for nuclei in the valley of stability.

The isospin dependence can be investigated mainly in three ways: (i) by studying targets with different isospin asymmetry, ε , using the same projectile; (ii) by comparing the scattering of neutrons and protons from the same target (in which case the isovector term changes sign); (iii) by studying (p, n) reactions between isobaric analog states. In the first approach, ε increases with A , a correlation that makes it difficult to separate purely A -dependent effects, such as the A -dependence of the nuclear radius, from the isospin dependence [8]. A variation on this method is to study chains of isotopes or isotones, in which A changes relatively little, but ε changes significantly. Unfortunately, nuclear structure also varies significantly across such a chain, producing changes in V_r not directly related to isospin dependence. This confuses such an analysis, making it impractical for isolating the isovector components of a global potential.

The second approach to investigating the isospin dependence is to parametrize (p, p) and (n, n) scattering consistently. Since isovector contributions to the potential are of opposite sign for the two projectiles, while nuclear structure effects and A -dependence are often similar (especially for nuclei away from closed shells), such a procedure should be more reliable. This is the method that we chose.

The third method, the analysis of (p, n) reactions, would isolate the isovector potential, but there are not sufficient high-quality data in the appropriate A - and E -ranges to justify inclusion in our analysis.

We assume, as usual, that the isovector terms V_t and V_{te} in eq. (2.11) affect only the potential depth and not the geometry. This assumption does not necessarily hold [3], but, given the small contribution of the isovector terms to the depth (less than 3 MeV), their effects on the geometry would be difficult to determine from elastic scattering. The isovector energy dependence, V_{te} , is included for completeness. The evidence for the energy dependence of the isovector potential is weak; some studies require none [24] but others do [23]. We eventually found (sections 4 and 6) that V_{te} in eq. (2.11) is not significantly different from zero.

Folding-model calculations should reliably describe the radial form of the real central potential, especially in the low-density region outside the nuclear surface. We observed in such calculations (section 2.1) that the half-density radius of nuclear density distributions, and therefore of the resulting folding potentials, do not obey the simple $A^{1/3}$ dependence usually assumed in optical-model analyses. This effect is a fundamental property of diffuse nuclear form factors [15] and has long been known from

electron-scattering determinations of charge radii [43]. Density dependence in the effective interaction also modifies this deviation from the $A^{1/3}$ dependence [10, 15]. By using the charge- and matter-radius parametrization and the effective interaction (M3Y) described in section 2.1, we found that the half-density radius, R_0 , of the density-independent folded potentials can be reliably parametrized as

$$R_0 = r_0 A^{1/3} + r_0^{(0)}, \quad (2.12)$$

with $r_0 = 1.24$ fm and $r_0^{(0)} = -0.70$ fm. Failure to include the offset $r_0^{(0)}$ in a global analysis significantly affects the determination of the isovector and Coulomb correction components of the optical potential. We chose the diffuseness of the real central potential to be independent of A and E , since folding-model calculations suggest only a slight but non-systematic A -dependence, presumably reflecting the shell dependences of surface thicknesses. A constant diffuseness, representing the average over our sample of nuclei, $a_0 = 0.56$ fm, was selected as the starting value for the initial parameter searches.

2.4. Coulomb potential and Coulomb correction

For proton scattering the potential must include a realistic Coulomb potential and its effects on $V(r)$. Coulomb effects appear in the potential as the electrostatic term of eq. (2.4) and as a Coulomb correction term E_c in eq. (2.11). Since the Coulomb interaction is relatively slowly varying compared with the total real potential, such that in ^{120}Sn it varies by about 5 MeV from $r = 0$ to $r = R_0$ while the nuclear potential varies by 25 MeV, approximate methods may be used to calculate it.

2.4.1. Coulomb potential for a diffuse charge

We modeled the Coulomb potential as that from a sphere of radius R_c with charge Ze uniformly distributed throughout its volume. In applying this potential to proton scattering we chose R_c so as to produce at the nuclear surface an electrostatic force very close to that from a 2pF charge distribution with radius R_{cd} , eq. (2.1). This choice is sensible because over the range of proton energies considered scattering is most sensitive to the surface region. To obtain the electric field at $r = R_{cd}$, we made [14] the leptodermous approximation $a_{cd}/R_{cd} \ll 1$, where a_{cd} is the diffuseness parameter of the 2pF charge distribution, eq. (2.1), and kept terms through second order in this ratio. We obtained the equivalent uniform-potential radius by equating this field to that from a uniform charge density confined within R_c . This results in

$$R_c(A) \approx R_{cd}(A) + 1.040a_{cd} + \frac{4.089a_{cd}^2}{R_{cd}(A)} \text{ fm}. \quad (2.13)$$

Inserting our previously described parametrization of nuclear charge radii (eq. 2.1) into the above, gives

$$R_c(A) \approx 1.238A^{1/3} + 0.116 \text{ fm}, \quad (2.14)$$

for the equivalent sharp Coulomb radius to model the Coulomb potential. In deriving this we replaced R_{cd} in the last term of eq. (2.13) with its average value of 5.03 fm for the range $40 \leq A \leq 209$, making an error of less than 2% in $R_c(A)$.

In previous analyses, constant Coulomb radii (usually $R_c = 1.25A^{1/3}$ fm) were often used. Although the numerical values given by these formulas make only small differences in the final potential parameters, our procedure is justified by the physics of the Coulomb potential and allows R_c to be fixed.

2.4.2. Coulomb correction to proton energy

The presence of the Coulomb potential in (p, p) scattering complicates consistent parametrization of (p, p) and (n, n) scattering, because the optical potential is momentum dependent [7, 16, 22]. Therefore, in a semiclassical description of the scattering, the repulsive Coulomb force reduces the incident proton kinetic energy. Thus, the average optical potential for a proton of given bombarding energy corresponds to that of a neutron with lower incident energy. The best method to account for these Coulomb effects in the optical potential would be to solve the Schrödinger equation with a momentum-dependent optical potential, resulting in an integral equation that is time-consuming to solve [7, p. 450] and for which it is not clear what form of momentum dependence to use.

The usual approach is to make a Coulomb correction [22, 44] to the depth of only the real potential and to assume a linear energy dependence of the potential depth on the incident energy, as in eq. (2.11). The latter assumption is justified for energies far above the Fermi energy [45], which are at least 15 MeV in our analyses.

If the imaginary potential is momentum dependent, it too should have a Coulomb correction [46]. One prescription [24] assumes that the energy of an incident proton is reduced by E_c . In evaluating E_c in eq. (2.12), we have used the same radius parameter as in the Coulomb potential. For a linear energy dependence of the potential, this gives equivalent results to the Perey model [22]. Therefore, for proton scattering, E_c in eq. (2.11) was chosen as

$$E_c = \alpha \frac{6Ze^2}{5R_c}, \quad (2.15)$$

where the coefficient α allows scaling of E_c relative to the average Coulomb energy. This procedure gives the same parametrization of the Coulomb correction for the real potential as the Perey model ($\alpha = 1$) and can be applied consistently to the absorptive potential. We eventually found (sections 4 and 6) that $\alpha = 1$ produces consistently good fits to our global database.

The importance of a correct treatment of the Coulomb corrections is apparent, since $V_c E_c$ in eq. (2.11) is typically about twice as large as the isovector potential term ϵV_c . We note a convenient inconsistency in $E - E_c$; E is in the laboratory frame, but E_c is in the centre-of-mass frame. This has no practical consequences in view of the smallness of such differences for $A \geq 40$ and the approximate nature of the Coulomb correction terms.

The Coulomb correction has been studied previously by comparing (n, n) and (p, p) scattering at similar incident energies on $N = Z$ nuclei. Such comparisons have been made for scattering from ^{28}Si , ^{32}S , and ^{40}Ca [8]. The results of such comparisons have significant uncertainties [46] because of nuclear structure effects. From this type of study it is not possible to deduce the radial form factor for the correction, although it is expected to differ significantly from the form factors for the nuclear potential [3]. When making Coulomb corrections, we assume the same radial dependences for them as for the neutron central potential.

2.5. Spin-orbit potential

Most analyses of low-energy scattering and most model calculations are consistent with a spin-orbit potential that is essentially real at $E \leq 65$ MeV [47]. Guided by folding-model calculations (section 2.1), it is usually taken to have the Thomas radial form [7, p. 457; 26]. However, its strength comes mostly from the spin-orbit part of the effective nucleon-nucleon interaction, rather than from relativistic effects.

Our folding-model calculations of the spin-orbit potential included exchange effects, and were made for proton scattering at 16 and 65 MeV. The results for the depth were parametrized as

$$V_{\text{so}} = V_{\text{so0}} + V_{\text{soe}}E + V_{\text{soA}}A^{-1/3}, \quad (2.16)$$

and for the geometry as,

$$R_{\text{so}} = r_{\text{so}}A^{1/3} + r_{\text{so}}^{(0)} \quad (2.17)$$

with a_{so} constant, since it varied slightly but non-systematically with A and did not vary with E . The parametrization of the spin-orbit radius, including the offset radius $r_{\text{so}}^{(0)}$, reflects the behavior of the radius of the underlying density distributions. The predicted parameter values from the folding model $V_{\text{so0}} = 5.1$ MeV fm², $V_{\text{soe}} = -0.0087$ fm², $V_{\text{soA}} = 5.61$ MeV fm², $r_{\text{so}} = 1.24$ fm, $r_{\text{so}}^{(0)} = -0.82$ fm, and $a_{\text{so}} = 0.66$ fm, were used as starting values in the optical-model parameter search, which will be described in section 4. Eventually (section 6), no clear signatures of E - or A -dependences were found by the fitting, so a single value of V_{so} is quoted. Its value of 5.9 MeV is essentially the folding-model prediction for the energy and mass midpoints of the database, $E \approx 30$ MeV, $A \approx 120$.

Since the nucleon-nucleon spin-orbit interaction (effective or real) has a range somewhat less than the central potential, folding models predict $R_{\text{so}} < R_0$. However, the absorptive-potential radius is at least as large as the central-potential radius, because of the peripheral nature of absorption. Therefore, the analyzing powers are quite sensitive to the complex central potential as well as to the spin-orbit potential.

2.6. Absorptive central potential

The imaginary central potential is usually represented as a combination of volume and surface-peaked form factors. Surface peaking of the form factor is expected if the dominant absorptive processes occur in the nuclear surface, for example, as collective excitations and transfer reactions [7, p. 457]. Such a form is also found in microscopic calculations of the imaginary potential [3, 48]. This peaking is most prominent for low-energy ($E < 20$ MeV) nucleon scattering, so that at low energies the nucleon wavefunction is damped on the nuclear surface, preventing it from sampling the nuclear interior and making the scattering insensitive to the interior potential.

For higher-energy projectiles the dominant absorption is from nucleon-nucleon collisions within the nuclear volume, related to the finite mean free path of nucleons in the nucleus [49, pp. 139, 165; 50]. This component of the absorption potential then resembles the bulk distribution of target nucleons and may be modeled by a Woods-Saxon form factor.

The imaginary part of the optical potential is difficult to calculate from semi-microscopic grounds. Calculations have been attempted in a nuclear structure framework [48], but the results are specific to

the nucleus under study. Nuclear matter calculations produce complex potentials, the absorption describing the finite free path of nucleons in nuclear matter [2]. However, this type of calculation neglects such absorption effects as collective excitations and reactions in finite nuclei. Therefore, to parametrize the absorptive potential we have been guided by phenomenology.

2.6.1. Phenomenology of absorptive potentials

There are two well-determined empirical characteristics of the absorptive potential. First is the transition from principally surface-dominated absorption at low energies ($E < 20$ MeV) to volume-dominated absorption at higher energies ($E > 60$ MeV). Second is that the proton optical potentials have imaginary volume integrals per nucleon, which are approximately constant as a function of A and E [17]. In addition, we imposed the physically reasonable criterion that the transition from surface to volume absorption takes place smoothly as a function of energy. Such a criterion was not applied in previous global analyses [1, 8] resulting in unphysical discontinuities in the potentials and their volume integrals as a function of E .

To account for the above observations, we needed energy dependences varying smoothly with E . We chose the energy dependence of the absorptive potentials as

$$W(r, E) = W_v(r) \left[1 + \exp\left(\frac{W_{ve0} - (E - E_c)}{W_{vev}}\right) \right]^{-1} + W_s(r) \left[1 + \exp\left(\frac{(E - E_c) - W_{se0}}{W_{sew}}\right) \right]^{-1} \\ = f_{vv}(E)W_v(r) + f_{vs}(E)W_s(r), \quad (2.18)$$

in which W_v and W_s are the depths of the imaginary surface and volume potentials. The parameters of the energy dependences are the half-value energies, W_{ve0} and W_{se0} , for the volume and surface absorptions respectively, and the widths, W_{vev} and W_{sew} . If $W_{ve0} = W_{se0}$ and $W_{vev} = W_{sew}$, the constancy with E of the absorption volume integral, J_w in section 2.1, is satisfied automatically for any A , since the surface and volume terms are assumed to have the same geometry. Examples of the volume integrals are shown in fig. 1. The form eq. (2.18) has been used previously [51, 52] and satisfies the criterion of smoothness in E .

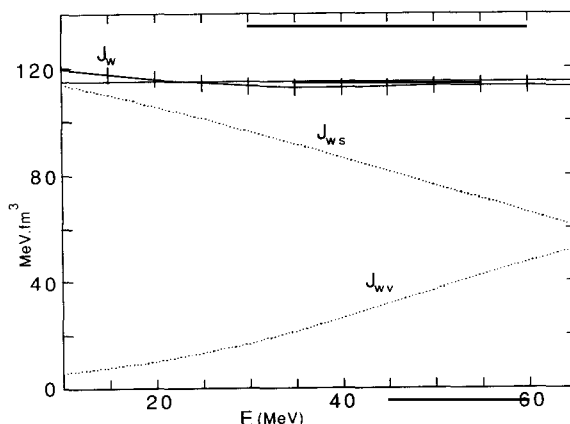


Fig. 1. Energy dependence of the absorptive potential for CH89. The volume integrals of the surface (J_{ws}) and volume (J_{wv}) absorptions are shown by dotted lines and the total absorptive volume integral ($J_{ws} + J_{wv}$) is shown by a solid line. The calculations are made for proton scattering from $A = 125$, $Z = 50$ at $E = 30$ MeV. Coulomb corrections are included in the calculation. The phenomenological observation of ref. [17] is indicated by the horizontal solid line.

To investigate parametrizations that reflect the approximate constancy of J_w/A with A , consider the expressions for these integrals in eq. (2.7). For the surface terms, a constant value can be maintained if W_s rises to compensate the fall as $A^{-1/3}$ of $1/R_w$. This can be described by including an isovector term in the potential depth, by introducing an A - or ϵ -dependent diffuseness [1, 53], or from the density dependence of the effective interaction similar to that of the real potential [3]. Usually, W_v is assumed to be isoscalar for consistency with results from medium-energy proton scattering [18].

3.6.2. Parametrization of absorptive potentials

From the considerations in section 2.6.1, we chose the following parametrization of the imaginary central-potential depths:

$$\begin{aligned} W_v &= W_{v0} f_{wv}(E), \\ W_s &= (W_{s0} + W_{st} \epsilon) f_{ws}(E), \\ R_w &= r_w A^{1/3} + r_w^{(0)}, \end{aligned} \tag{2.19}$$

with a_w a constant. Here f_{wv} and f_{ws} are the energy-dependent factors in eq. (2.18). The potential radius has an offset from the usual parametrization as a function of $A^{1/3}$, in analogy with the real central and spin-orbit components of the potential (sections 2.3 and 2.5). This offset is necessary if there is a density dependence of the imaginary parts of the effective interaction [10, 15].

As discussed in section 2.4, the proton Coulomb correction for the imaginary central potential was applied in the same manner as for the real central potential, by reducing the proton energy at which the potential is evaluated by E_c [given in eq. (2.15)]. It is not clear [48] that such a procedure is well justified, since the available channels for absorption will differ for protons and neutrons, even when the energy has been adjusted. However, one expects that when the nuclear energy is well above the thresholds for significant nucleon-absorption channels the procedure will be reasonable. In fact, our global analyses indicate little sensitivity to the absorptive Coulomb correction because of the two complementary dependences on E_c in eq. (2.18).

3. Database of nucleon elastic scattering

We now describe the database assembled from recently available accurate data for use in the global optical-model analysis outlined in section 2. In particular, we establish the criteria for inclusion of data in the database in section 3.1 and we discuss the breadth and quality of the data assembled, using as an example in section 3.2 the 16 MeV proton scattering data we measured at Triangle Universities Nuclear Laboratory (TUNL). The other contributions to the database are described in section 3.3.

3.1. Database criteria

An important ingredient of a global parametrization is the breadth in the database of (p, p) and (n, n) scattering. The data we selected for analysis were measured at only a few laboratories to reduce systematic problems and distinguish such problems from effects arising from the parametrization.

The proton data were from TUNL ($E = 16$ MeV) [14] and three other sources; Eindhoven University

of Technology ($E = 17$ to 25 MeV) [54, 55], Oak Ridge National Laboratory (ORNL) ($E = 40$ MeV) [56, 57], and the Research Center for Nuclear Physics (RCNP), Osaka, Japan ($E = 65$ MeV) [58, 59]. All the proton data were measured using polarized beams, and in most cases the $\sigma(\theta)$ and $A_y(\theta)$ data were measured simultaneously. The neutron data were from two sources, the σ and A_y data from the TUNL neutron time-of-flight facility ($E = 10$ to 17 MeV) [60–63] and the σ -data from the Ohio University Accelerator Laboratory (OUAL) ($E = 11$ to 26 MeV) [64]. To minimize database errors, we used only data available in tabular form.

Figure 2 summarizes the A - and E -distributions of this database, which is the largest body of data ever assembled for an optical-model analysis. There are approximately 6000 (p, p) σ and A_y data, in 95 data sets each containing both observables, with average statistical uncertainties of less than 2%. There are about 3000 (n, n) data in 60 data sets of mostly elastic σ -data, with 15 sets of A_y data. The (p, p) and (n, n) data are for target nuclei $40 \leq A \leq 209$, using nucleon beams with energies $10 \leq E \leq 65$ MeV, under which criteria compound-elastic contributions are probably negligible [16]. The experimental conditions for the measurements at each laboratory are summarized in table 4, and the nuclei investigated are tabulated in table 5.

We present samples of the data with fits from the global analysis in figs. 3 to 11. The data sets shown are usually composed of an angular distribution of σ/σ_R and $[\sigma/\sigma_R]A_y(\theta)$ for (p, p), where σ_R is the Rutherford cross section, and of $\sigma(\theta)$ and $A_y(\theta)$ (where available) for (n, n).

For each target nucleus in the (p, p) data the A_y data were converted into *analyzing cross sections* (cross sections times analyzing powers), σA_y , half the difference between the left-hand and right-hand scattering cross sections with a beam fully polarized along the normal to the scattering plane. This observable is preferable to A_y , since theoretically A_y is computed from it by dividing by σ . Using A_y ,

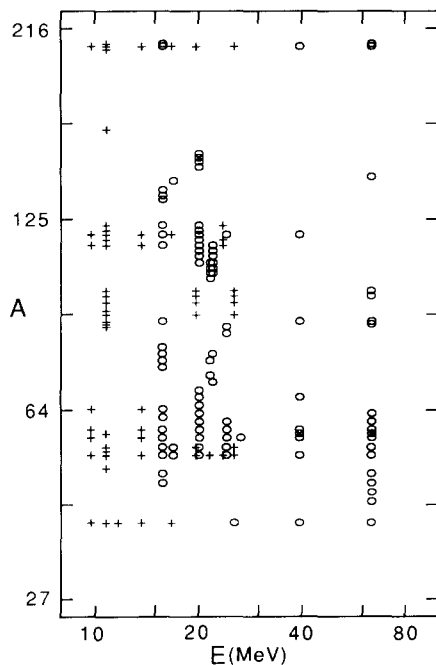


Fig. 2. Distribution of targets in the nucleon scattering database in target mass (A) on an $A^{1/3}$ scale and incident nucleon energy (E) on a logarithmic scale. Values of A and E for which we used data are indicated for proton scattering by circles and for neutron scattering by plus signs.

Table 4
Experimental conditions for the (p, p) and (n, n) data used in the CH89 optical-model potential

	Protons				Neutrons	
	TUNL, [14]	Eindhoven, [55]	ORNL, [56, 57]	RCNP, [58, 59]	TUNL, [60–63]	OUAL, [64]
E_{lab} (MeV)	16.0 ± 0.05	$(17-27) \pm 0.1$	40 ± 0.4	65.0	$(10-17) \pm 0.1(\sigma) \pm 0.3(A_y)$	$(11-26) \pm 0.1$
Uncertainties:						
Relative						
$\sigma(\theta)$	1–3%	2–3%	1–10%	1–5%	5–20%	3–5%
$A_y(\theta)$	<0.01	<0.01	0.1–0.15	<0.04	<0.07	–
Normalization						
$\sigma(\theta)$	$\leq 6\%$	$\leq 10\%$	5%	1–20%	5%	5%
$A_y(\theta)$	5%	5%	5%	1%	2.5%	–
$\Delta\theta_{\text{det}}$ (deg)	± 0.6 – ± 1.2	± 1 – ± 2	± 0.4 (σ) ± 1.2 (A_y)	–	^{a)}	^{a)}

^{a)} This angular acceptance is corrected in the multiple-scattering calculations used to analyze the data.

an error in fitting σ is reflected in A_y . For example, at cross-section minima, significant enhancements in A_y often occur, which are not directly related to spin-orbit potential effects. For elastic scattering in the energy range considered here, σA_y is a more uniform function of angle than is A_y , and we found that the contribution to the error-weighted residuals from σA_y is closer to that from σ than that from A_y , because σA_y is bounded by $-\sigma$ and σ . Thus, polarization observables in the σA_y form have a more equitable weighting in the fitting process discussed in section 4.3.

The standard deviation for σA_y was estimated by using the uncorrelated propagation of errors form,

$$\Delta(\sigma A_y) = (A_y^2 \Delta\sigma^2 + \sigma^2 \Delta A_y^2)^{1/2}, \quad (3.1)$$

where $\Delta\sigma$ and ΔA_y are the standard deviation estimates in σ and A_y . We investigated correlations between σ and A_y that might significantly alter the magnitude of this uncertainty when these are measured simultaneously, since σ and A_y are computed from the same independent variables, the counts in the left and right detectors. A detailed analysis [14] shows that the effects of such correlations are negligible for the data used here.

The neutron data are represented as σ and A_y . Accurate conversion of A_y into σA_y could not be made, because the σ -data were not usually measured at the same angles as A_y . However, for the same reasons as for (p, p), it would be better to fit σ and σA_y rather than σ and A_y .

The (p, p) data are sparse between 25 and 65 MeV, because of the lack of accelerators with polarized beams in this energy range. However, this is the region where the transition from surface-dominated to volume-dominated absorption probably occurs. For the neutron data the problem is more severe, since there are no systematic data above 26 MeV because of a lack of neutron scattering facilities. In addition, there is a large gap between $A = 124$ and $A = 208$ at all energies (see fig. 2), partly because of insufficient energy resolution in proton and neutron detection systems for elastic scattering from most nuclei in this mass range.

There were also problems with individual data sets, most significant of which are normalization problems, since some proton data were originally normalized to optical-model calculations. The inaccuracies possible with these techniques and the effects of improper normalization on parameter determination are discussed in section 4.3.2. This can be a serious problem at higher energies [57],

Table 5
Elastic-scattering data sets for the CH89 optical-model potential database. Units are incident nucleon energy in MeV

Target nucleus	(n, n)		(p, p)			
	TUNL	OUAL	TUNL	Eindhoven	ORNL	RCNP
⁴⁰ Ca	10, 14, 17	11			40.0	65.0
^{44,48} Ca						65.0
⁴⁶ Ti						65.0
^{48,50} Ti			16.0			65.0
⁵¹ V		11				
⁵⁵ Mn		11				
⁵⁴ Fe	10, 14	11, 20, 22, 24, 26	16.0	17.2, 20.4, 24.6	40.0	65.0
⁵⁶ Fe		11, 20, 26	16.0	17.2, 20.4, 24.6		65.0
⁵⁹ Co		11			40.0	65.0
⁵⁸ Ni	10, 14		16.0	20.4, 24.6, 27.2	40.0	65.0
⁶⁰ Ni	10, 14		16.0	20.4, 24.6	40.0	65.0
⁶² Ni				20.4, 24.6		65.0
⁶⁴ Ni				20.4		65.0
⁶³ Cu			16.0			
⁶⁵ Cu	10, 14		16.0			
⁶⁸ Zn				20.4	40.0	
^{64,66,70} Zn				20.4		
^{72,74} Ge				22.0		
^{78,80} Se			16.0	22.3		
^{76,82} Se			16.0			
⁸⁶ Sr				24.6		
⁸⁸ Sr		11		24.6		
⁸⁹ Y		11				65.0
⁹⁰ Zr		11	16.0		40.0	65.0
⁹³ Nb		11				
^{92,96} Mo		11, 20, 26				
^{98,100} Mo		11, 20, 26				65.0
^{106,108,116} Cd				22.3 ^{a)}		
^{110,112,114} Cd				20.4, 22.3 ^{a)}		
¹¹⁶ Sn	10, 14	11, 24	16.0	20.4		
¹¹⁸ Sn		11, 24		20.4		
¹²⁰ Sn	10, 14, 17	11	16.0	20.4, 24.6	40.0	
¹²² Sn		11		20.4		
¹²⁴ Sn		11, 24	16.0	20.4		
^{132,134,138} Ba			16.0			
¹⁴² Nd				17.2 ^{a)}		
¹⁴⁴ Sm						65.0
^{148,150} Sm				20.4 ^{a)}		
¹⁶⁵ Ho		11				
²⁰⁶ Pb		11				
²⁰⁸ Pb	10, 14, 17	11, 20, 26			40.0	65.0
²⁰⁹ Bi		11				65.0

^{a)} These data were normalized by us.

where the same data set with different normalizations can be described equally well by quite different potentials.

3.2. Polarized proton data from TUNL

As an example of the procedures used to acquire accurate elastic scattering data for the database, we summarize our measurement of the 16 MeV data. Details are given in ref. [14] and about half of these

data are shown in figs. 3 and 4. We used several criteria to select 23 target nuclei, among which were: (i) a wide range of target mass ($40 \leq A \leq 209$), (ii) many chains of isotopes for investigating isospin effects, and (iii) matching of targets to proton data at other energies and to neutron data. Compromises were necessary for two principal reasons.

First, many potentially interesting targets required target-making techniques and processing beyond our capabilities. Second, the detector system and electronics had a resolution of greater than 50 keV

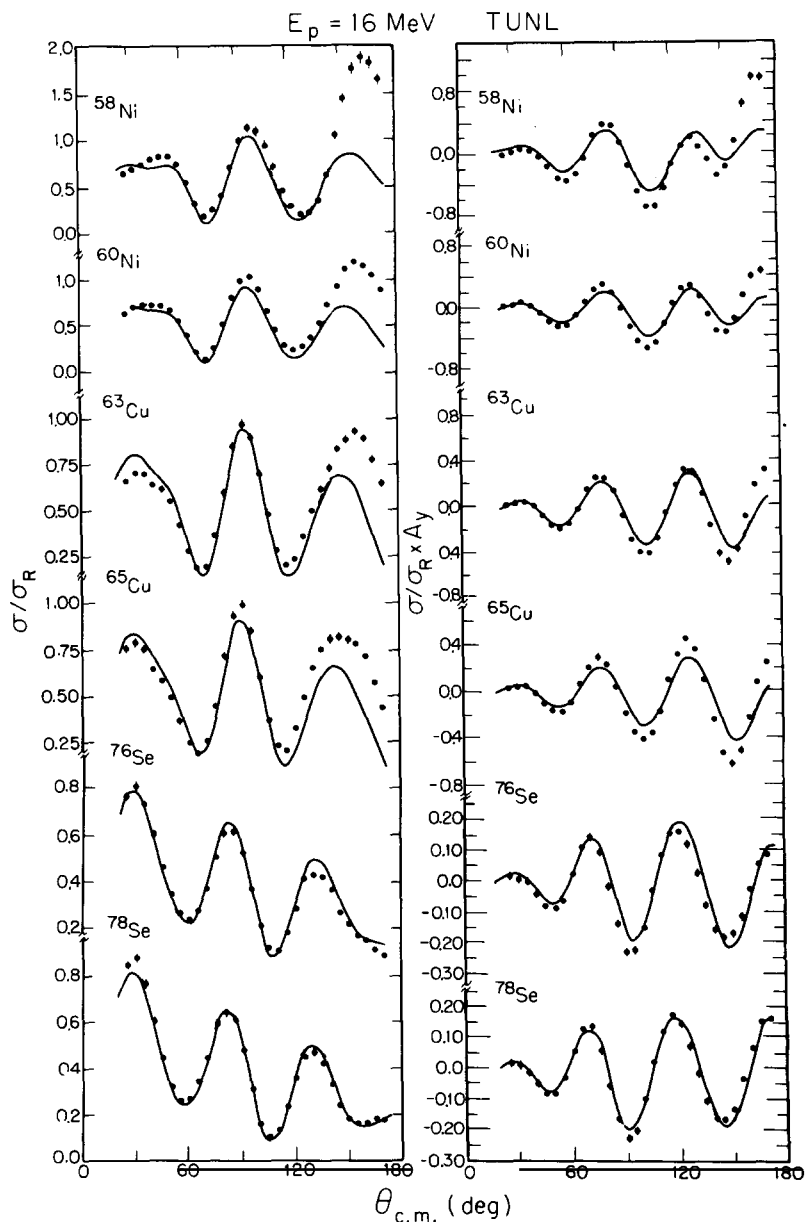


Fig. 3. Proton elastic scattering, measured at TUNL, using 16 MeV polarized protons. Uncertainties are shown where they are larger than the data points. The lines are the optical-model predictions using the best-fit potential parameters of CH89. Less than half of all the angular distributions we used are shown in figs. 3–11.

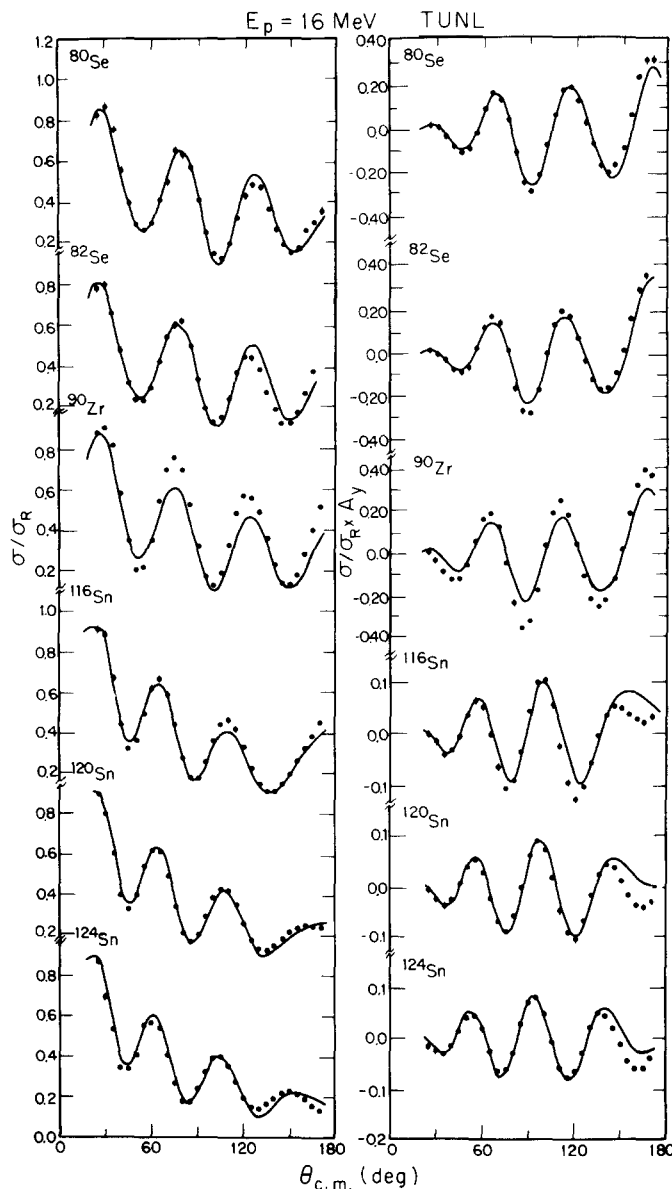


Fig. 4. Proton elastic scattering data and CH89 fits for 16 MeV polarized protons, measured at TUNL. See fig. 3 for details.

(FWHM). This effectively prevented our measuring reliably elastic scattering on nuclei for which the excitation energy of the first-excited states is less than 100 keV, such as most rare-earth nuclei. However, nuclei near closed shells have relatively high-lying first-excited states, so the targets we selected (and those used in previous global analyses) emphasized nearly-closed-shell nuclei [1, 8]. Of our 23 targets at 16 MeV, 19 are within one nucleon of a closed neutron or proton shell. Our targets overlap significantly with those of other data sets used in our global analysis, and the database reflects the same experimental constraint towards closed-shell nuclei.

3.2.1. The data acquisition scheme

The 16 MeV (p, p) data are $\sigma(\theta)$ and $A_y(\theta)$ measured simultaneously using essentially the same detector geometry and experimental procedure for each target, at laboratory angles between 25° and 170° in 5° steps.

Each A_y measurement was made in two steps, with the beam spin up, then down, and with detectors placed symmetrically left and right of the beam. This scheme eliminates most first-order errors in A_y [65] and is the standard scheme at TUNL for A_y measurements. The differential cross section was measured simultaneously with A_y , and was calculated as the uncertainty-weighted mean of the cross sections from spin-up and spin-down steps.

The 16 MeV polarized proton beam was produced in a Lamb shift polarized-ion source [66], then accelerated in an FN tandem Van de Graaff electrostatic accelerator. The beam for these experiments had an average polarization of 80% and an average intensity of 80 nA at the target. The energy spread of the beam on target was less than 10 keV, with an absolute energy uncertainty of less than 50 keV [67].

The scattering chamber contained two sets of detectors, one set each on the top and bottom rotating plates. Each set was separately adjusted in scattering angle to maintain left and right symmetric detector placement while the chamber vacuum of 9×10^{-6} mbar was maintained. The four detector holders in each set were pinned into the plates, 10° apart, at a radial distance of 15.9 cm from the target, ensuring reproducibility of position and angle. The angles could be set to a precision of better than 0.1° ; the alignment was checked optically with the actual detector holders used. The detectors were silicon surface-barrier detectors with defining apertures subtending angles of 0.6° to 1.2° and with solid angles of 1.3 msr to 2.5 msr. To facilitate measurements near 90° with the symmetric detector placement, the target angle was continuously variable from 0° to 180° , and could be set reliably to within 0.5° , adding uncertainties of less than 1% in the data.

The beam polarization was monitored with an active polarimeter using the well-determined A_y of the ${}^4\text{He}(p, p){}^4\text{He}$ reaction [68], placing left and right detectors at $\theta = 112^\circ$, where A_y is a maximum. The polarimeter detectors were plastic scintillation detectors because they did not become radiation damaged at 16 MeV as quickly as solid-state detectors. The beam dump was well separated from the monitor, and it incorporated a split Faraday cup with secondary electron suppression to provide beam position information for keeping the beam centered on the target and polarization monitor. This monitor was calibrated using solid-state detectors in place of the scintillators. For the 16 MeV beam used in this work and with the backgrounds present in the monitor detectors, the monitor analyzing power was $A_y = 0.92 \pm 0.04$.

We investigated potential sources of error in beam current integration, among which were: (i) failure to capture all the beam because of the small size of integration surfaces, (ii) inadequate suppression of secondary electrons, (iii) loss of captured beam current because of leakage current to ground, and (iv) inaccuracies in the beam current integrator. We made tests and calculations to estimate these uncertainties. None contributed more than a 1% uncertainty to the $\sigma(\theta)$ measurements.

The pulse-height signals from the right-left detector pairs were processed together using standard electronics and stored in a DEC VAX 11/780 computer, which ran the TUNL XSYSstem data acquisition and analysis software [69]. The dead time was measured actively by injecting a slow (10 Hz) pulser into the test input of one detector preamplifier of each detector pair. The maximum dead time of 10% arose in the signal-shaping electronics, largely from pile-up rejection. The system was very stable, exhibiting no detectable gain changes over measurement periods of up to 4 h. The energy linearity of the system was better than 1%.

3.2.2. Target thickness measurement

Most of our 23 targets were vacuum evaporated. They were either self-supporting or supported on thin carbon films. Their thicknesses ranged from $100 \mu\text{g cm}^{-2}$ to $800 \mu\text{g cm}^{-2}$, as measured using Rutherford or near-Rutherford scattering of 4 to 6 MeV protons. At these energies, an optical-model description of $\sigma(\theta)$ at forward-scattering angles ($<40^\circ$) is insensitive to details of the parametrization, producing less than 1% uncertainties in the $\sigma(\theta)$ normalizations. The low-energy scattering was performed in the same experiment as the 16 MeV scattering, using the same detector geometry. The product of target thickness and detector solid angle thus determined contributed the largest uncertainty to $\sigma(\theta)$. Multiple measurements of the product of thickness and solid angle, using the same detector at different scattering angles, gave values varying from 2% to 5%. Comparison with optical-model calculations and other elastic-scattering data at 16 MeV suggested discrepancies averaging 4% or less.

A few of the targets, namely ^{50}Ti and $^{134,136}\text{Ba}$, were significantly contaminated by other isotopes. Also, ^{54}Fe was contaminated by significant amounts of NaCl during the target production. These angular distributions were carefully corrected for these contaminants, as detailed in ref. [14].

3.2.3. Data uncertainty estimates

The importance of determining correct relative and absolute (normalization) uncertainties for optical-model studies is discussed in section 4.3.2. We worked carefully to estimate realistic uncertainties for the 15 MeV polarized (p, p) data.

Relative uncertainties arose mainly from statistical uncertainties in counting, statistical uncertainties in pulser-based dead-time-correction estimates, and from less easily measured fluctuations, such as non-uniformity in the target thickness or variations in beam angle and position on target. Other contributions to relative uncertainties arose in determining the relative detector solid angles, or uncertainties in target orientation relative to the beam. In the 16 MeV measurements uncertainties from counting statistics were 1% or less in $\sigma(\theta)$; the corresponding uncertainties in $A_y(\theta)$ were generally 0.01 or less. Dead-time correction uncertainties were always less than 1% and, to first order, affected only $\sigma(\theta)$.

Straightforward statistical estimates of $\sigma(\theta)$ uncertainties proved inadequate for the 16 MeV data. We compared measurements with different detectors at the same angles, using our best estimates of relative detector and beam current normalizations. The standard deviations of these comparisons were significantly larger than our purely statistical estimates of uncertainty, so we used the mean of the comparison standard deviations as an estimate of the instrumental or systematic uncertainties. We calculated the total relative uncertainty by adding these instrumental uncertainties in quadrature with the counting-statistics uncertainties as

$$(\Delta\sigma/\sigma)^2 = (\Delta\sigma/\sigma)_{\text{statistical}}^2 + (\Delta\sigma/\sigma)_{\text{systematic}}^2, \quad (3.2)$$

because the overlapping measurements used to estimate uncertainties were at forward-scattering angles where statistical uncertainties were negligible compared to the estimated instrumental uncertainties. At more backward-scattering angles it was necessary to account for statistical uncertainties, which should enter approximately independently of instrumental uncertainties.

A similar procedure was followed for the A_y data. We estimated the instrumental uncertainty from the mean of the standard deviation of A_y measured with different detectors at the same angle. For A_y data these estimated instrumental uncertainties were generally smaller than the statistical uncertainties. The uncertainty for each A_y was then computed as

$$\Delta A_y^2 = \Delta A_y^2(\text{statistical}) + \Delta A_y^2(\text{systematic}). \quad (3.3)$$

To estimate normalization uncertainties, we evaluated several possible contributions. The uncertainties in σ are composed of uncertainties in the detector solid angle and target thickness, absolute angle, and average efficiency of beam-current integration. Uncertainties in target thickness, based on standard deviations of repeated measurements, ranged from 1% to 6%. Only the uncertainty in thickness contributed significantly to the normalization uncertainty. For A_y data the only significant uncertainty in normalization was from the beam-polarization determination. As discussed above, except for statistical uncertainties in the polarimeter data (<1%), the only normalization uncertainty in polarization was in the effective monitor analyzing power, about 4%.

There are two ways to investigate the absolute uncertainties. The first is to compare our data with other measurements of elastic scattering at 16 MeV. We did this using σ -data measured previously on $^{58,60}\text{Ni}$, ^{90}Zr , ^{120}Sn , and ^{208}Pb [70], which have a stated accuracy of about 2%. The TUNL $\sigma(\theta)$ data agreed with those of ref. [70] within 5%. An alternative measure of reliability of the σ -normalizations is the renormalization estimated from comparison of the forward-scattering angle data with optical-model predictions. For small renormalizations (<5%), studies with synthetic data (sections 4.2 and 4.3) show that this normalization factor can be estimated reliably by optical-model calculations. Renormalizations suggested by optical-model fits to each target data set are generally small, on the order of 1%.

In view of these comparisons, and to assure realistic accuracy in the data, we used a uniform normalization uncertainty of 5% for all the 16 MeV polarized (p, p) σ -data. We used a uniform normalization uncertainty of 4% for the A_y data, based on the determination of the monitor analyzing power, since we did not locate comparable A_y measurements and an optical-model comparison is not appropriate.

3.2.4. TUNL data excluded from the database

Three of the 16 MeV scattering data sets exhibit significant resonant behavior. The nuclei ^{208}Pb and ^{209}Bi exhibit strong isobaric analogue resonances [71] near 16 MeV. Some previous optical-model analyses had included ^{208}Pb proton scattering near 16 MeV and ignored the resulting inconsistency of the potential at this energy with that at other energies [70, 72].

We experienced similar problems in fitting the $^{40}\text{Ca}(p, p)^{40}\text{Ca}$ data. A previous attempt [52] to describe the 16 MeV data with an energy-dependent optical model for ^{40}Ca , found that the 16 MeV optical potential was inconsistent with ^{40}Ca parameters at other energies. Other attempts at such analyses experienced serious difficulty with ^{40}Ca elastic scattering data near the (p, n) threshold at 16.2 MeV [73]. In addition, reaction cross-section measurements show oscillatory behavior near 16 MeV, just before the (p, n) threshold [73]. Because of such non-direct (p, p) scattering from these three nuclei, we decided to exclude these data from the global database.

3.3. Other data for the database

The measurement conditions for the data sets other than the TUNL 16 MeV proton scattering (section 3.2) are summarized in table 4, and all the nuclei used are listed in table 5. We now characterize these data.

3.3.1. The Eindhoven proton 17 to 27 MeV data

The data for 17 to 27 MeV polarized (p, p) scattering consist of 42 pairs of σ and A_y angular

distributions. They were obtained [74] from an extensive elastic and inelastic scattering database measured at the Eindhoven University of Technology. The facilities and procedures used are described elsewhere [54, 55, 75]. About one quarter of the Eindhoven data for our database are shown in figs. 5 and 6.

The $\sigma(\theta)$ data were normalized by comparison with optical-model calculations, and were estimated to be accurate to 5% by minimizing the best-fit estimator with respect to a single data normalization factor [54, 76]. In particular, the technique used in the Eindhoven analyses was to estimate this factor after each iteration of the optical-model search program.

Some of the data we received were only approximately normalized, requiring us to re-estimate their normalization. It was not appropriate for us to use the Eindhoven method [54], because of our search algorithms, as described in sections 4.3 and 4.4. Instead, we estimated the renormalization by making

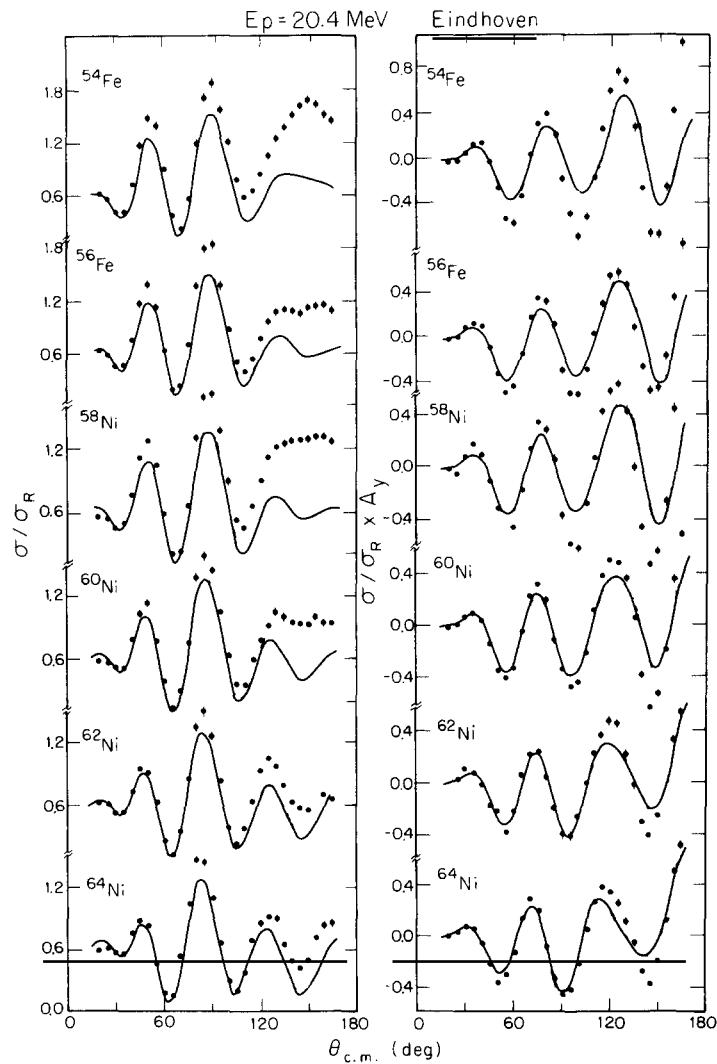


Fig. 5. Proton elastic scattering data and CH89 fits for 20.4 MeV polarized protons, measured at Eindhoven. See fig. 3 for details.

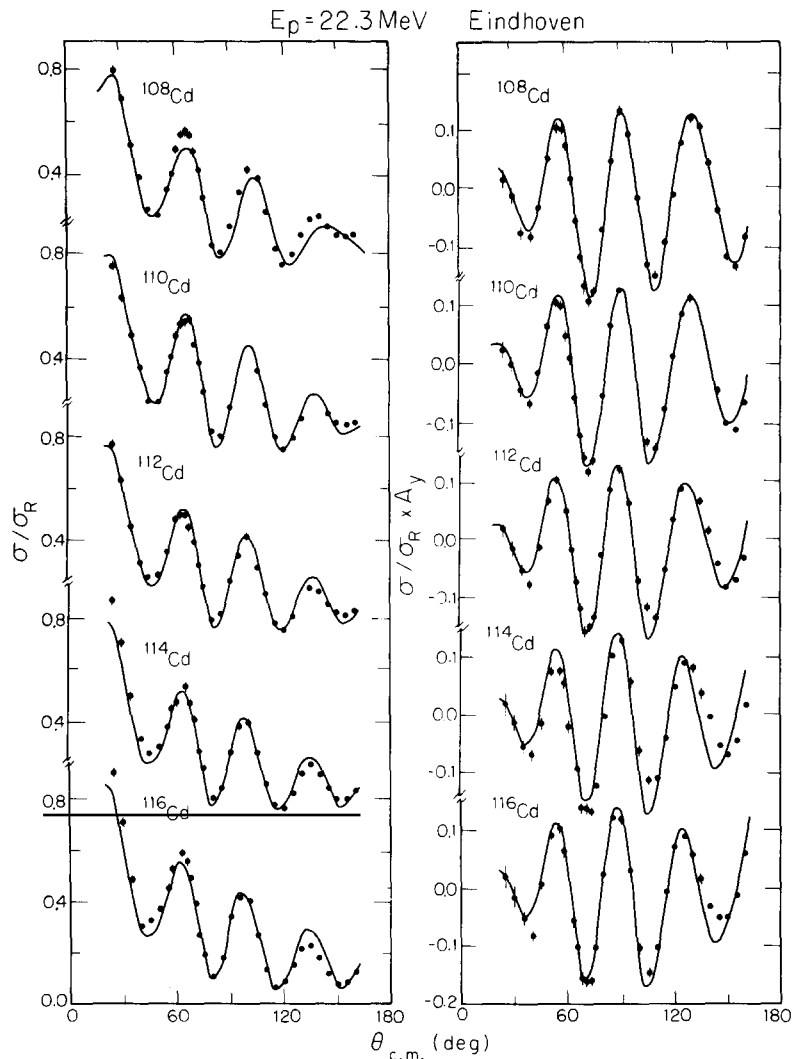


Fig. 6. Proton elastic scattering data and CH89 fits for 22.3 MeV polarized protons, measured at Eindhoven. See fig. 3 for details.

optical-model fits to the individual data sets, then allowing the optical-model program to estimate a best-fit renormalization. This technique was not reliable for all data sets. We fitted the data for ^{110}Pd and several Sm isotopes using renormalization factors that differed from unity by 10% to 20%, in an attempt to find the appropriate factor. The fits with various renormalization factors differed significantly in the minimum value of the least-squares function. The optical-model calculations, however, consistently estimated a renormalization factor of unity. Thus, for these data, the estimate of the renormalization from the optical-model calculation was accurate to only about 20%. To compensate for this failure of the technique, we estimated the normalization from the forward angle $\sigma(\theta)$ data. Even this was unreliable for ^{110}Pd and $^{152,154}\text{Sm}$, so we excluded these data from the database searches.

3.3.2. The ORNL proton data at 40 MeV

The data for 40 MeV proton scattering were obtained from Oak Ridge National Laboratory (ORNL)

[53, 56, 57]. These data are nine angular distributions of $\sigma(\theta)$ and $A_y(\theta)$ measured at $E = 40$ MeV. Most of these data are shown in fig. 7.

The polarized proton beam was produced by scattering an 81 MeV alpha-particle beam from an H_2 gas target, using recoil protons at an angle of 25.5° (with a polarization of 0.89), or by scattering an unpolarized 41 MeV proton beam from a ^{40}Ca target at an angle of 25° (with a polarization of 0.27). The advantage of the Ca polarizer was its higher efficiency and the solid target, which provided a beam with better energy resolution than by alpha-particle scattering. Most measurements were made with the Ca polarizer.

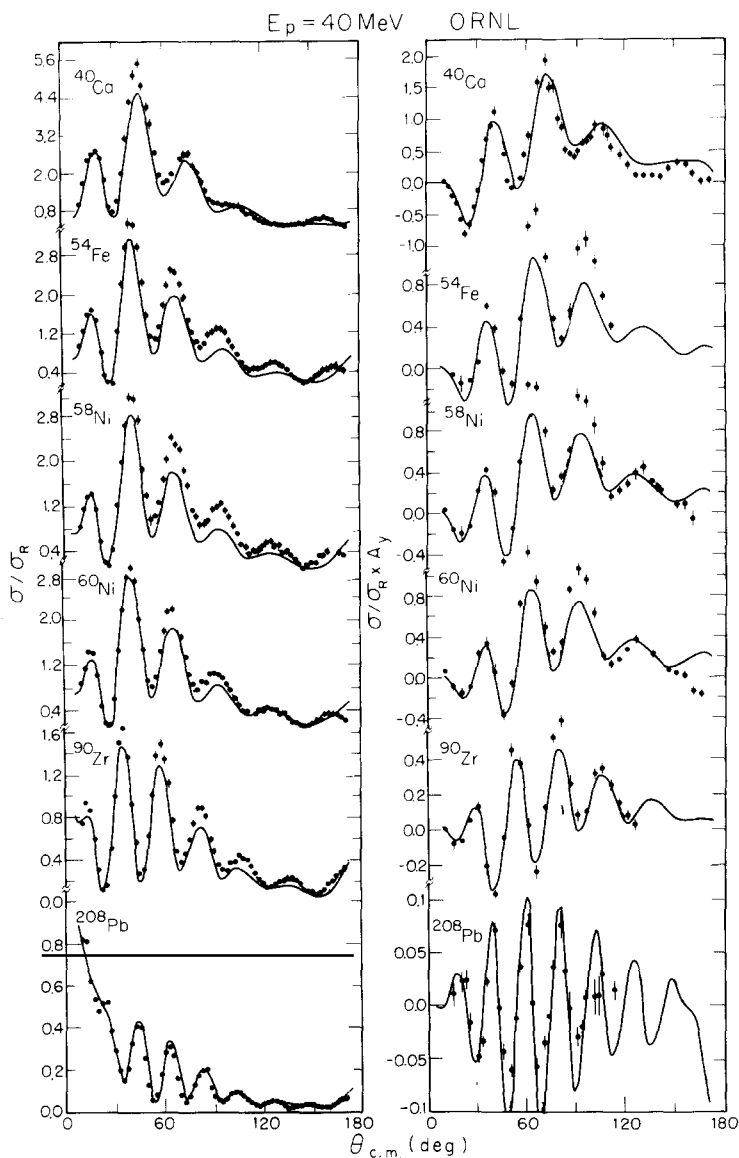


Fig. 7. Proton elastic scattering data and CH89 fits for 40 MeV polarized protons, measured at ORNL. See fig. 3 for details.

The ORNL $\sigma(\theta)$ and $A_y(\theta)$ data were measured in separate experiments because of the low intensity of the polarized beam. The σ -measurements were made in steps of 2.5° , while A_y was measured with left-hand and right-hand detector pairs in angle steps of about 5° [57]. The target thicknesses were determined by energy-loss measurements with a 20 MeV ^3He beam, normalizations determined after the initial publication of the data [53]. Because of difficulties in determining the beam polarization, these data have been assumed to have a 5% normalization uncertainty in both σ and A_y .

3.3.3. The RCNP proton data at 65 MeV

The data for 65 MeV proton scattering were obtained from the large (p, p) data collection measured at the Research Center for Nuclear Physics (RCNP) [58, 59]. The σ -data and A_y data were measured

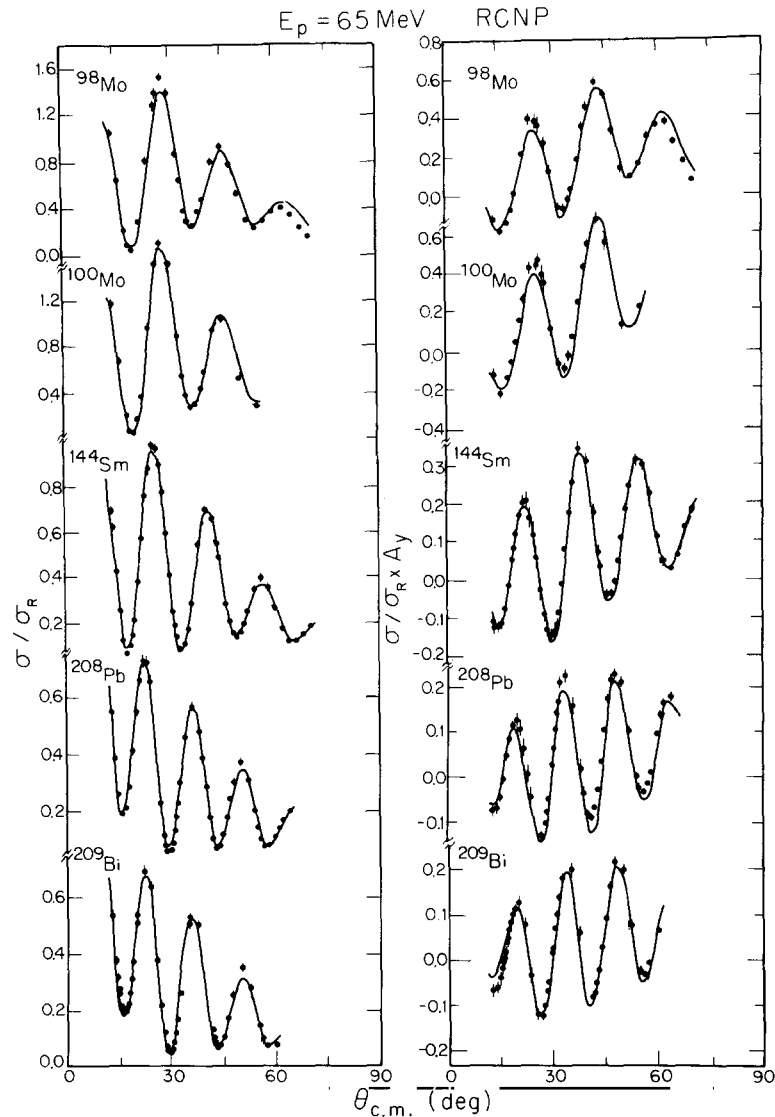


Fig. 8. Proton elastic scattering data and CH89 fits for 65 MeV polarized protons, measured at RCNP. See fig. 3 for details.

simultaneously with a polarized proton beam, using left–right detector pairs. The σ data were normalized by weighting the targets to obtain the target thickness and by measuring the detector geometry to compute the solid angle [59]. Subsequently, the authors renormalized the σ -data to best-fit optical-model calculations. Estimated uncertainties are given in table 4, the target nuclei are indicated in table 5 and about one-quarter of the 19 RCNP data sets are shown in fig. 8.

3.3.4. The TUNL neutron data for 10 to 20 MeV

The polarized neutron scattering data were obtained from the neutron time-of-flight facility at TUNL [60–63]. This facility is uniquely capable of measuring polarized neutron scattering in the 10 to 20 MeV

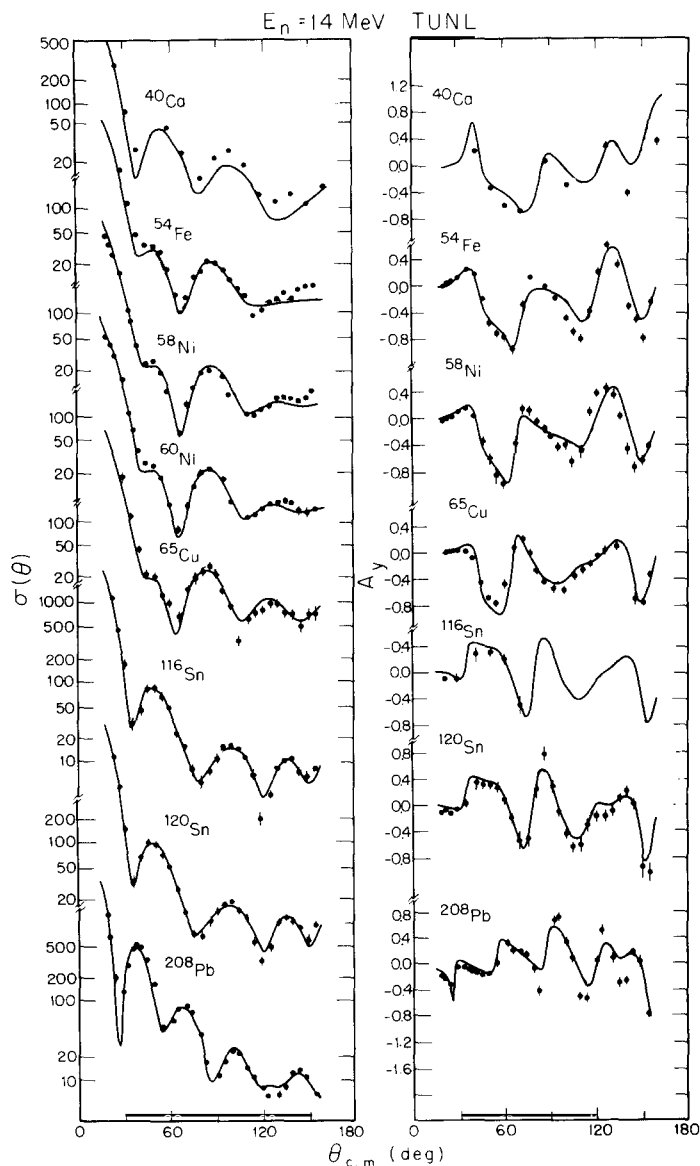


Fig. 9. Neutron elastic scattering data and CH89 fits for 14 MeV polarized neutrons, measured at TUNL. See fig. 3 for details.

energy range. The techniques used to measure elastic and inelastic scattering at this facility have been thoroughly described elsewhere [61, 62], especially the multiple-scattering corrections required because of the large targets used in the low incident flux. The target nuclei measured, the energies used, and the estimated uncertainties are given in tables 4 and 5. Of the 19 TUNL neutron angular-distribution sets about half are shown in fig. 9.

3.3.5. The OUAL neutron data for 10 to 26 MeV

The unpolarized neutron $\sigma(\theta)$ data were measured at the Ohio University Accelerator Laboratory (OUAL) in the energy range 10 to 26 MeV. We obtained these data from the National Nuclear Data Center at Brookhaven National Laboratory. They have been published previously [64] and some have been used in an optical-model analysis of neutron scattering [8, 23]. The targets, energies, and estimated uncertainties are given in tables 4 and 5. One third of the 36 OUAL $\sigma(\theta)$ distributions are shown in figs. 10 and 11.

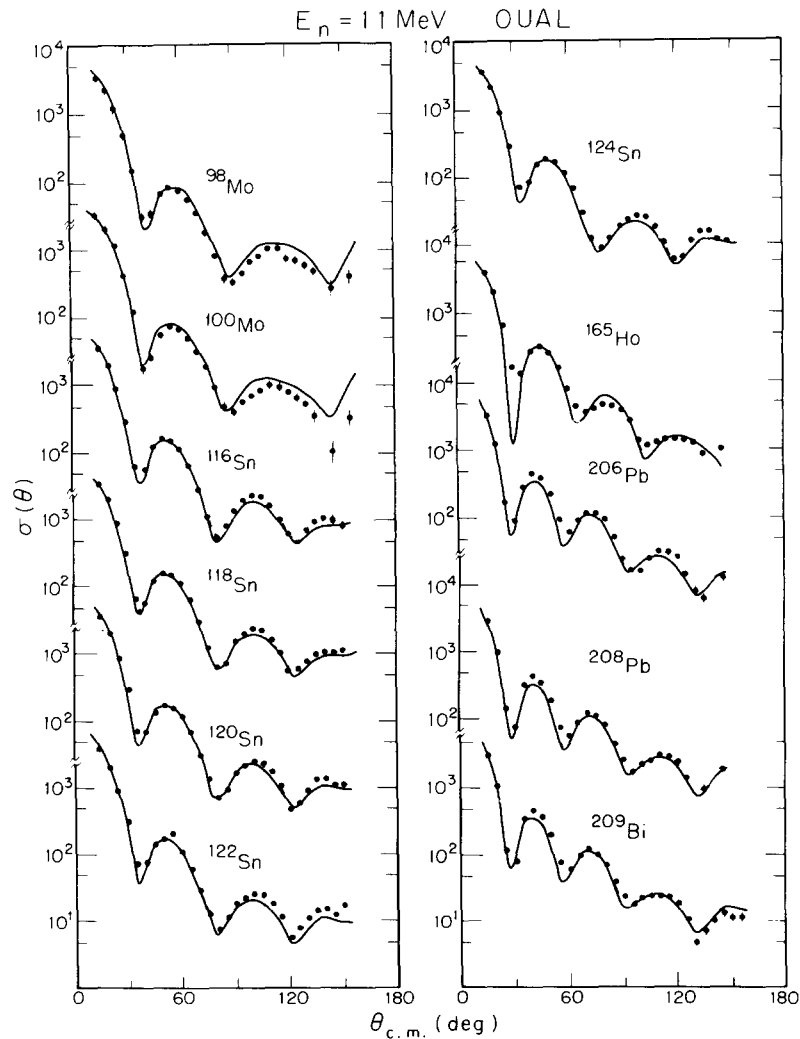


Fig. 10. Neutron elastic scattering data and CH99 fits for 11 MeV neutrons, measured at OUAL. See fig. 3 for details.

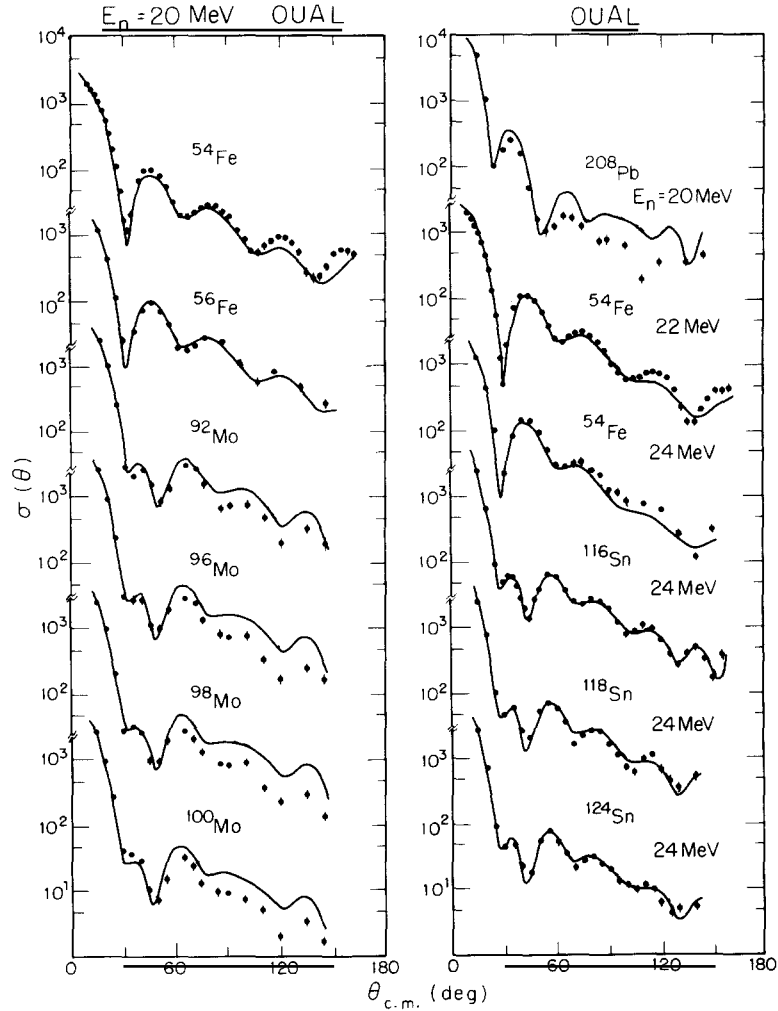


Fig. 11. Neutron elastic scattering data and CH89 fits for 20 to 24 MeV neutrons, measured at OUAL. See fig. 3 for details.

4. Optical-model analysis procedures

In our analysis of elastic scattering data in the global optical model we used a potential parametrized to reflect current understanding of the optical potential, as summarized in sections 1.4 and 2. Our analysis procedure therefore focused not on experimentation with different forms of potential parametrization, but on eliminating terms in the chosen parametrization (section 2) that are not well determined by the data, finding the best values of the remaining parameters reliably, then estimating the uncertainties in these parameters.

We sought the optical set of 20 optical-model parameters for the potential described in section 2 to describe the 292 angular distributions of σ and A_y in our database (section 3). To do this we needed a fast, accurate, and efficient optical-model program, since more than 60 000 separate optical-model calculations were typically made in a single global parameter optimization. The procedure had to search

without human guidance, more than a dozen correlated parameters in a highly non-linear model, since we know of no way that a human can compare data and predictions in 292 angular distributions and reliably decide how to change the global parameters.

We also needed a function to describe the quality of fit, such that the best fit would be found unambiguously. When the fit was found we needed to estimate the parameter confidence limits and correlations between parameters. Such estimates have been absent in past analyses, yet they are an essential guide to users of the parameters.

To meet these requirements we constructed the program MINOPT (see section 4.1) from the programs OPTICS, a nuclear optical-model program [76], and MINUIT, a minimization program [34]. Tests of the suitability of MINOPT for optical-model parametrizations are described in section 4.2. The use of least squares as the goodness-of-fit estimator is justified in section 4.3. Finally, the search procedures are summarized in section 4.4. The method used to estimate the uncertainties is reserved for section 5, while the results of the analysis are given in section 6.

4.1. The optical-potential search program MINOPT

Two programs were combined to produce MINOPT [14] – an optical-model program, OPTICS, and a function-minimization program, MINUIT. In the following we summarize their features, then in sections 4.2 and 4.3 we describe how MINOPT was used in the global-parameter analysis.

4.1.1. The optical-model program OPTICS

The program OPTICS is a small, efficient nuclear optical-model program for computing elastic scattering observables for light structureless projectiles of spins 0, 1/2, or 1 [76]. OPTICS numerically solves the Schrödinger equation containing the optical potential described in section 2.2. It predicts σ and A_y (or σA_y), then compares them with the corresponding data by calculating a goodness-of-fit function. The numerical integration technique used is a modified Numerov method [77]. The time-intensive parts of OPTICS were optimized for best performance on each of the several computers used.

Many features in OPTICS make it ideal for use in global searches. It automatically adjusts the matching radius and the maximum partial wave in a calculation to help minimize the calculation time in searches over a wide range of incident energy and target mass. The σ and A_y (or σA_y) data are allowed to have different weights in calculating the best-fit estimators. OPTICS can renormalize data, using the current optical-model calculation to estimate the minimum of the least-squares function for the data set with respect to its normalization [76]. We preferred this technique to that used in some optical-model programs, in which the normalization is adjusted after each iteration of the search program [54]. The latter normalization adjustment reduces considerably the value of the iterative minimization techniques we used (section 4.1.3), which assume that there is no change in the shape of the parameter space during the search. The net effect of such “on-the-fly” renormalization is to confuse the search and slow the convergence significantly.

OPTICS can include Mott–Schwinger (magnetic-dipole scattering) corrections to neutron scattering. We observed that these corrections have no significant effect at most angles where neutron analyzing powers are measured, so they were excluded from this analysis because they increase the computation time.

4.1.2. The optimization program MINUIT

To perform the work of parameter optimization we adopted MINUIT, the well-developed minimiza-

tion system from CERN [34], rather than writing our own optimization program. The development of such programs requires much experience in the numerical properties of various optimization algorithms, and a variety of different algorithms that are effective at different distances from the minimum of the quality-of-fit function should be employed. These features exist in MINUIT, and are well documented for users [34]. MINUIT is also capable of automatically switching between algorithms when there appear to be problems with the convergence of the search.

4.1.3. Minimization algorithms in MINUIT

The procedures used in MINUIT for optimization (function minimization or point estimation) are described in detail elsewhere [34, 78, 79]. These are implemented such that we only need to provide a function whose value is a minimum when the best optical-model fit has been obtained. We discuss in section 4.3 our choice of that best-fit function. The various routines for function minimization in MINUIT are applicable under different assumptions about the function to be minimized and the quality of the fit at the search starting point, as we now summarize.

A *Monte Carlo* technique of randomly sampling points in the parameter space is used when there is no prior knowledge of the best-fit function or the starting point in parameter space.

The *simplex* algorithm [34, 79] is used when the starting point is relatively far from the best fit. It depends only on successive evaluations of the best-fit function, and makes no assumptions about its shape, such as being parabolic in each parameter, which might hold only near a minimum. The simplex algorithm works by calculating the quality-of-fit function at $n + 1$ points in a minimization with n parameters (forming a simplex in the n -dimensional space), then searching along a line from the worst-fit point through the center-of-mass of the other n points. The algorithm specifies three alternative steps, one to outside the simplex, one twice as far in the same direction, or one inside the simplex. The best of the new points, that with the minimum function value, is added to the simplex, and the worst-fit point is discarded. The method is stopped when the step sizes are below a user-specified minimum.

The simplex method is very robust, but gives little information about the curvature of the function, so it may have trouble near a minimum by stepping back and forth over the optimum values. We used the simplex when starting searches from a completely new set of parameters. This algorithm is also invoked by MINUIT when there are problems with the convergence of the variable-metric method.

The *variable-metric* method, which we used most often for optimizing parameter values, is a gradient-based method [34], which finds roots of the gradient of the quality-of-fit function, Q^2 (section 4.3), with respect to the parameters. This is done by making a quadratic approximation of Q^2 in terms of each varied parameter, which holds only close to a minimum [78]. From this assumption an estimate of \mathbf{p}_{\min} , the parameter set that minimizes Q^2 , may be found from the expression,

$$\mathbf{p}_{\min} = \mathbf{p}_0 - \mathbf{V}^{-1} \mathbf{g}, \quad (4.1)$$

in which \mathbf{p}_0 is the current set of parameter values, the covariance matrix \mathbf{V} is the inverse of the matrix of second derivatives of Q^2 with respect to the parameters, and \mathbf{g} is the gradient of Q^2 evaluated at \mathbf{p}_0 .

In the variable-metric method \mathbf{V} is not directly evaluated at each iteration, which would be time consuming and not always useful at any significant distance from the minimum, since this is a quadratic approximation. Instead, it makes an initial approximation to \mathbf{V} , exactly evaluates the gradient, then searches for a minimum along the direction predicted by eq. (4.1). The approximate covariance matrix is corrected after each iteration by an updating formula, which includes the result of the search. This

technique is generally very stable, and it produces a covariance matrix that may be used to estimate parameter confidence limits and correlations [34]. The variable-metric method stops when the estimated distance to the minimum and the average fractional change in the covariance are both less than user-specified values.

4.2. Studies using synthetic data

Early in the development of MINOPT, we studied the suitability of MINUIT for the problem of global optical-model parameter determination, particularly its consistency and stability. Tests were also made to evaluate alternatives to least-squares as a quality-of-fit function. To best carry out these tests, a global database was needed that could be well described by the optical model and for which the best possible fit was known without question.

The tests we developed used a set of synthetic data, generated from an arbitrary, global optical-model potential. The source potential was a realistic potential based on preliminary fits to proton elastic scattering. The calculated data sets were 16 MeV proton scattering from ^{60}Ni , ^{90}Zr , ^{120}Sn , ^{138}Ba and ^{208}Pb . For each target nucleus, optical-model angular distributions of $\sigma(\theta)$ and $\sigma A_y(\theta)$ were calculated in 5° steps from 25° to 170° . This closely emulated the 16 MeV TUNL proton scattering data (section 3.2), thus facilitating later comparison of the tests and actual fitting. For calculating the quality-of-fit function, arbitrary, uniform uncertainties of 2% for $\sigma(\theta)$ and of 0.01 for $A_y(\theta)$ values were assigned; these were then combined in the same manner as uncertainties for the true data (section 3.2.3) to generate uncertainties in σA_y .

To provide test data that simulate problems typical of the elastic-scattering databases we used (section 3), we modified the synthetic database in two ways. First, we multiplied each data point by a random noise factor, distributed normally with a standard deviation of 0.05 and mean of unity. We did not change the assigned uncertainties after the addition of noise, reflecting the usual experimental situation, in which one's knowledge of uncertainties is incomplete, a lack that can influence the estimate of the best fit. Secondly, we modified each angular distribution by multiplying it by a random renormalization factor. These factors were normally distributed with a standard deviation of 0.05 and a mean of unity, one factor for each angular distribution. The uncertainties assigned are representative of those for our 16 MeV (p, p) data described in section 3.2. The modifications to the synthetic database provided a very realistic test of the search methods, especially for effects resulting from database deficiencies.

4.2.1. Tests of MINOPT stability

We tested MINOPT stability by starting a search from parameter values relatively far from the source potential and then observing the program behavior in finding the best fit to the synthetic data. The starting parameters were selected by three different prescriptions: (i) 10% changes in components of the potential (real, imaginary or spin-orbit), leaving all the other terms at their optimum values, (ii) changing 11 of the potential parameters away from their optimum values by a constant fraction (e.g., 10%), and (iii) changing the potential parameters to exploit the known parameter correlations in the optical potential, such as $V_r R_0^2$, $W_s a_w$, and $V_{so} R_{so}$ [6]. Such choices of starting parameters provided a reproducible means of biasing the searches.

The synthetic data studies were made using the variable-metric method, minimizing the sum of the best-fit function Q^2 (section 4.3) from both the $\sigma(\theta)$ and the $\sigma A_y(\theta)$ data, searching for 11 parameters simultaneously. The studies revealed that stability of the search requires careful selection of starting

values of the real central-potential parameters. In general, searches that started with the real potential depth, radius, and diffuseness parameters more than 5% different from the generating potential would not converge in a search, and would produce parametrizations that did not fit the data well. Such fits corresponded to local minima in regions distant from the true potential, often referred to as “discrete ambiguities” [6].

4.2.2. Tests of search strategies

For starting potentials with real terms less than 5% different from the source potential, tests with the synthetic database showed that two types of strategies were useful: (i) searching for all parameters simultaneously, and (ii) searching separately on the central and spin-orbit potential. If the search converged successfully, strategy (i) was preferable, yielding final parameter values close to the best-fit potential in the least time. When strategy (i) failed to converge, the more complex strategy (ii) generally succeeded. Use of this search method usually produced a potential parametrization close enough to the best-fit potential to enable use of strategy (i) in a subsequent search.

Uniform, upward renormalization of all data sets by 5% did not affect the ultimate parametrization, although subsequent estimates of the renormalizations were generally not correct. If the σ -data were renormalized by 10%, the search would not converge, showing the importance of correct cross-section normalization to about the 5% level, which is about the level attained by our database (section 3). Even if MINOPT did not signal that it had converged to a minimum, it usually had reached a potential close to the source potential. This highlights a caution in dealing with this search algorithm in MINUIT, that several search iterations are required before there is enough information to detect convergence.

4.3. Best-fit estimators

Once we were generally satisfied with the behavior of the optimization software, we had to choose a quality-of-fit function that would enable us to find the best parametrization efficiently. This function is referred to in statistics as an estimator. A major deficiency of MINUIT and most automated fitting procedures is that only a single number is used to characterize fit quality. The obvious choice of this estimator is the sum of error-weighted residuals squared, that is,

$$Q^2 = \sum_{i=1}^N \frac{[x_i - T_i(\mathbf{p})]^2}{\Delta x_i^2}, \quad (4.2)$$

in which x_i denotes an element of the set of N data, $T_i(\mathbf{p})$ is the optical-model prediction for the datum x_i based on the vector of parameters \mathbf{p} , and Δx_i is the estimated standard deviation of the measured x_i . Estimation of the best values of the parameters by minimizing Q^2 is called the “method of least squares”.

If each term of Q^2 is normally distributed with a standard deviation of one and a mean of zero, Q^2 has a χ^2 distribution. From this distribution the reliability of the extracted parameters can be calculated. This has led to the goodness-of-fit measure Q^2 being often referred to as “ χ^2 ”, although this is not generally true [80]. To clarify this difference, and because we found (sections 5.1.3, 6.2) that Q^2 did not have these desirable properties for our global parametrization, we have named it differently.

For the global optical-model potential, we thought that the least-squares method might hinder finding the best fit, especially because of the effect of outlying data points on fit quality. The minimum Q^2 value, Q_{\min}^2 , has significant contributions from data that the model is not able to describe, such as

changes in angular distributions from strong channel coupling or from systematic errors. These contributions could easily mask effects of adjusting the optical model to fit the majority of data that are well described.

We therefore examined two other goodness-of-fit functions, which might reduce the emphasis of such outlying points:

$$\sum_{i=1}^N \max(0, \ln\{[x_i - T_i(\mathbf{p})]^2 / \Delta x_i^2\}), \quad (4.3)$$

$$\sum_{i=1}^N |[x_i - T_i(\mathbf{p})] / \Delta x_i|. \quad (4.4)$$

These functions make a calculated value far from a data point contribute less strongly than to Q^2 . In function (4.3), the logarithmic transformation could make negative contributions to the goodness of fit, so it is constrained to be positive. The function (4.4) has been mentioned [80] as a possible fitting function, especially when the tail of the underlying distribution of parameters is wider than the usually assumed normal distribution.

These goodness-of-fit functions were tested with synthetic data similarly to those described in section 4.2, for the least-squares function (eq. 4.2). In all cases tested, the convergence of the simple Q^2 function was much faster than that of the alternative functions in eqs. (4.3) and (4.4). Searches using these new fitting functions tended to be relatively insensitive to the best-fit potential parameters; we had succeeded too well and had lost sensitivity to even the good data.

In view of these negative results, we tested modifications to the fitting function that added information to Q^2 , particularly information about the relative phase between data and calculation, to which visual fitting is usually sensitive. To measure the relative phases, we programmed a comparison of the locations of extrema in the calculated and measured angular distributions, including this information with the Q^2 function as a penalty term [34]. This strategy hindered rapid convergence of the fit; our technique was inaccurate at locating extrema because of the relatively large angular separations of the data points for many of the data sets compared to the separation of extrema. Consequently, we chose to stay with the least-squares criterion, the minimization of Q^2 in eq. (4.2), to measure the quality of fitting.

4.3.2. Least squares and data normalization

In our preliminary fits of a global optical potential to the database (section 3), we observed that there were large contributions to the least-squares function Q^2 from data that either cannot be well described by any optical model (such as data with compound elastic scattering) or that might have substantial errors in the assignment of data uncertainties. For some data sets Q_{\min}^2 values were relatively large, even when individually fitted by an optical-model potential. An example is the $^{90}\text{Zr}(\text{p}, \text{p})^{90}\text{Zr}$ data set at 16 MeV. The best individual optical-model fit to these data was visually quite good, but Q_{\min}^2 was much larger than the average for the entire database. This arose from unusually small estimated uncertainties in these data. For the 16 MeV data, an estimate of the instrumental uncertainties was included in the variances, as discussed in section 3.2. For other data sets, excepting the RCNP data, the uncertainties are purely statistical.

To address these problems, the contribution of the j th angular distribution, Q_j^2 , to the global Q^2 function, $Q^2(\text{global})$, was renormalized by dividing it by $Q_j^2(\text{min})$ obtained in a local (non-global)

optical-model fit. Thus, for N_d data sets, we have

$$Q^2(\text{global}) = \sum_{j=1}^{N_d} Q_j^2 / Q_j^2(\text{min}). \quad (4.5)$$

This procedure approximately accounts for both factors mentioned above, namely, the validity of the optical model and the error in the data uncertainties. It is not difficult to obtain such fits, since we were not interested in globally consistent values of such optical-model parameters. Where possible, we compared our fits and the associated $Q_j^2(\text{min})$ values with those published for the data sources in section 3.3. They were usually similar. The reciprocals of the $Q_j^2(\text{min})$ values were used as the weights for each data set in the global fits.

The results of this weighting procedure are that each data set in the global parametrization contributes unity to $Q^2(\text{global})$ when the global model fits as well as the local model used for $Q_j^2(\text{min})$, and all the data sets in $Q^2(\text{global})$ are equally weighted. Although this procedure requires extra work, it is a realistic way to obtain global parameters unbiased by data uncertainties that have been inappropriately estimated. No attention was given to this consideration in previous global optical-model analyses.

4.4. Search procedures

There were two components to our search procedure; (i) the selection of subsets of the data for various searches, and (ii) strategies in using the search program. We now summarize these two aspects.

4.4.1. Selection of data

Because of the enormous task of searching on the global database described in section 3, we initially performed restricted searches to establish reliable starting values for the global potential. We either selected data sets from large data sets at a single energy containing many targets, usually from a single laboratory, or we selected target nuclei with data at many energies, including both (p, p) and (n, n). In the first case, there were, for polarized proton scattering, the 16 MeV data (TUNL, 20 data sets), the 20.4 MeV data (Eindhoven, 22 data sets), the 40 MeV data (ORNL, 9 data sets), and the 65 MeV data (RCNP, 20 data sets); for neutron scattering we used the unpolarized-beam 11 MeV data (OUAL, 23 data sets).

Searches were performed for each set of data independently, with the intent of determining the energy dependence of the optical parameters by comparison of values at different energies. These searches helped establish starting values for the global searches (section 4.4.2). The advantage of using these data sets was that variances of the data are likely to be consistent within one laboratory. A significant disadvantage was that they were measured with only one projectile isospin and one incident energy. It was therefore difficult with such data sets to separate isospin, Coulomb, or A -dependent effects, as discussed in sections 2.3 and 2.4. Therefore, use of such data only guided the estimation of simple isoscalar potential terms.

To study the effects of energy dependence and isovector dependence on the global parametrization, we used data for single isotopes measured at several energies with both proton and neutron scattering. The best cases were isotopes of Fe (21 data sets), Ni (20 data sets), Zr (4 data sets), Sn (23 data sets), and Pb (8 data sets). As mentioned in section 3.2.4, nuclear structure variations may cloud the interpretation of such searches, but they provided our best starting parameters.

The first large database was formed by merging the single isotope data sets. This created a database that represented the full range of A , E , and projectile isospin in the global database. To these we added all the TUNL proton-scattering data, the RCNP data, and some neutron scattering data. The resulting database of 75 data sets was used to establish reasonable parameter values and to confirm the convergence properties of MINOPT (sections 4.1, 4.2) for a global database. The ultimate global database contained 155 data sets.

4.4.2. *Final fitting methods*

From the synthetic-data studies (section 4.2) and subsequent work with the global database (section 4.4.1), it became clear that a simple strategy in MINOPT searches is the best, that is, allow it to search simultaneously on as many parameters as appear well determined by the data. Whenever the search seems unstable, the number of parameters must be reduced; elimination of the spin-orbit potential parameters from the search is usually sufficient. In searching on the global database (as opposed to small subsets or the test data), such instabilities were never encountered.

Our approach differs from that used in other nucleon optical-model analyses, in which the search was guided by gradually increasing the number of parameters used, in an attempt to avoid optical-model ambiguities [8, 62]. In our searches on the global database using MINOPT, such procedures slowed convergence.

We began our global search with the postulated parametrization, initially derived from folding-model estimates and phenomenology (section 2). We made these searches on subsets of the global database, usually chosen to reflect strongly some property of the global model we wished to investigate, such as isospin dependence. After one or two searches (starting the second search from the end point of the first), the parameter values usually stabilized. We then examined the search results to determine the next step in the process, for example, removing poorly determined parameters from the search.

Once we had a reasonable idea of the results to expect from the subset searches, we used the entire global database, searching and refining as above, to obtain the final global parametrization. Uncertainties and parameter correlations were then estimated by the bootstrap statistical analysis described in section 5. The best-fit parameter values and their uncertainties are presented and discussed in section 6.

5. Estimating optical-model parameter uncertainties

The study of the nucleon-nucleus optical model has now reached a sophisticated level in understanding its theoretical underpinnings (sections 1.4.1 and 2) and in the precision of elastic-scattering observables (as in section 3). Therefore, it is now desirable to estimate reliably the uncertainties of the optical-model parameters and the correlations between them. These quantities help to assess the significance of comparisons of theoretical models of the optical potential (section 2.1) with empirical potentials, as well as to gauge the reliability of predictions derived from these potentials. However, there has been no previous systematic attempt to evaluate global optical-model parameter uncertainties and correlations.

In the following subsections we review relevant concepts from statistics and probability theory (section 5.1), we introduce and illustrate the bootstrap method (sections 5.2, 5.3), then in section 5.4 we show how we applied it to estimate parameter uncertainties and correlation coefficients.

5.1. Relevant statistics and probability theory

The usual idea of a statistical uncertainty is that repeated measurements of a quantity vary randomly about its expectation value (mean value). These measurements have a distribution, and one sometimes uses its width as an estimator of the uncertainty. The width of the distribution is taken from the interval, centered on the mean, which contains a given fraction of the total probability for observing that quantity. Since the parameters of our optical-model potential are derived from data with uncertainties, they would have uncertainties even if the model were perfect.

A common measure of the uncertainty of a quantity x is the *standard deviation*,

$$\sigma = \left(\frac{1}{N} \sum_i (x_i - \bar{x})^2 \right)^{1/2}, \quad (5.1)$$

where \bar{x} estimates the mean value of x from N repeated measurements. If the distribution of the x_i over $i = 1, 2, \dots, N$ is normal (Gaussian) the standard deviation is the half-width of an interval that contains 68% of all the observations, that is, the probability $P(\bar{x} - \sigma < x < \bar{x} + \sigma) = 0.68$ [81]. For distributions that are not normal there is no a priori relation between the statistic σ and the probability P , a fact that is often ignored by physicists. As examples of non-normal parameter distributions, section 6.2 shows skewed distributions of optical-model parameters.

If two or more parameters are jointly (simultaneously) estimated, the probability statement for the standard deviation must be qualified, even for normal distributions. The probability content of the $\pm\sigma$ interval depends upon the estimates of all the other parameters [80]. Thus some estimates for the parameter x that are within $\pm\sigma_x$ of the mean \bar{x} are associated with other parameters y , with mean \bar{y} , which lie *outside* their $\pm\sigma_y$ interval. To make a statement about the joint probability of the n parameters requires evaluation of the joint n -dimensional probability distribution. Generally, the probability

$$P[(\bar{x} - \sigma_x \leq x \leq \bar{x} + \sigma_x) \cap (\bar{y} - \sigma_y \leq y \leq \bar{y} + \sigma_y)]$$

is much smaller than the individual probabilities for the x - and y -distributions separately. Such considerations lead to the notion of correlation coefficients.

5.1.1. Correlation coefficients and their uses

If two or more quantities are measured simultaneously, both the uncertainty in each and the degree to which variations in one parameter, x , can affect determination of another, y , should be described. The relation between x and y is usually described by the *correlation coefficient*, estimated by [81]

$$\rho(x, y) = \frac{\sum_i (x_i - \bar{x})(y_i - \bar{y})}{\left(\sum_i (x_i - \bar{x})^2 \sum_i (y_i - \bar{y})^2 \right)^{1/2}}, \quad -1 \leq \rho \leq 1, \quad (5.2)$$

in which the sum is over N repeated measurement pairs (x_i, y_i) . Here $\rho = +1$ indicates perfect correlation of x and y in the same direction, and if $\rho = -1$ they are correlated in opposition. Correlation coefficients are useful in two ways: (i) as a measure of the interdependence of two variables, and (ii) in the propagation of uncertainty for functions depending on both x and y .

For the optical potential, we can examine parameter correlations to discover which parameters are

closely linked and subject to the various ambiguities that plague optical-model parametrization. For example, given the observation that $V_r R_0^n \approx \text{constant}$ for the real potential is an ambiguity [6], we expect to see strong negative correlations between V_r and R_0 , indicating that a change in V_r can be compensated by a change of opposite sign in R_0 without significantly changing the quality of fit. Note that $\rho(V_r, R_0) = -n/|n|$ for the above ambiguity provided that the fractional variations of V_r and R_0 are not too large. Thus, $\rho \approx -1$ for *any* positive n .

When computing the uncertainty in a composite quantity, g , from two correlated variables, x and y , we should account for their correlation. Thus, the standard deviation of g , σ_g , is obtained from [81, p. 175]

$$\sigma_g^2 = \left(\frac{\partial g}{\partial x}\right)^2 \sigma_x^2 + \left(\frac{\partial g}{\partial y}\right)^2 \sigma_y^2 + 2 \frac{\partial g}{\partial x} \frac{\partial g}{\partial y} \rho \sigma_x \sigma_y. \quad (5.3)$$

We have verified that, to a very good approximation, g may be expanded about its mean value to first order in $x - \bar{x}$ and $y - \bar{y}$. Equation (5.3) is independent of the distributions of x and y , but the probability of an interval based on the calculated value of σ_g does depend on these distributions. This equation has a straightforward generalization to functions of more than two variables. At $\rho = \pm 1$, the extremes of the uncertainty,

$$\sigma_g = \left| \left| \frac{\partial g}{\partial x} \right|^2 \sigma_x^2 \pm \left| \frac{\partial g}{\partial y} \right|^2 \sigma_y^2 \right|^{1/2}, \quad (5.4)$$

are reached. For example, in the *local* optical model, with g a volume integral (section 2.2), x a potential depth and y its radius, ρ is close to -1 , so uncertainties in the volume integrals are much smaller than in depths and radii separately, in agreement with previous observations [26]. For the *global* optical model, section 6.2 shows that the correlation is weaker.

What values of ρ in eq. (5.3) are significant? Consider the common case in which g is formed from a product of powers of x and y . If the fractional uncertainties in x and y are comparable, then the fractional uncertainty in g is scaled by at most $(1 + \rho)^{1/2}$ relative to its value when correlations are ignored. More generally, when g is calculated from n parameters with fairly constant correlation coefficients between them (mean value $\bar{\rho}$), the fractional uncertainty is scaled by about $[1 + (n - 1)\bar{\rho}]^{1/2}$. For example, to make an error of less than 50% in the fractional uncertainty of the real central volume integral (in which there are six terms), one should include those parameter pairs having $|\rho| \geq 0.2$. As shown in section 6.2, uncertainties in estimating the correlations limit the precision of such calculated composite uncertainties.

5.1.2. Uncertainty estimates and probability

Estimates of the standard deviations and correlation coefficients are not useful unless the probability content of the interval, $p_i - \sigma_i \leq t_i \leq p_i + \sigma_i$, in which t_i is the “true” value of the parameter p_i , can be estimated. To do this one must either know, or assume, a probability distribution. For example, for the normal distribution there is a 68% probability that the true value of p_i is within $\pm 1\sigma$ of the most-probable value. For linear relations between data and parameters, normally distributed uncertainties in data imply normally distributed uncertainties in parameters. For non-linear relations, such as that between the elastic-scattering data and the optical-potential parameters, the probability distribution of parameters must either be assumed (parametric statistics) or determined using the

techniques of non-parametric statistics. We first discuss the normal-distribution statistics assumed for the error analyses provided by MINUIT [34, 78, 83], then in section 5.2 we describe bootstrap non-parametric statistics.

5.1.3. Relevance to optical-potential parameters

If we assume that the parameters, p_i , of the optical potential obey a normal distribution, then their standard deviations can be estimated from the covariance matrix, \mathbf{V} , calculated by MINUIT (section 4.1.3). The standard deviations of the parameters p_i are estimated as

$$\sigma(p_i) = \sqrt{V_{ii}}, \quad (5.5)$$

and their correlations with other parameters are estimated by

$$\rho(p_i, p_j) = V_{ij}/(V_{ii}V_{jj})^{1/2}. \quad (5.6)$$

MINUIT estimates of standard deviations and correlations are not obtained by directly examining the distributions associated with the parameters, but by assuming the parameters to be normally distributed and then relating σ of each distribution to the derivatives of the best-fit function, $Q^2(\text{global})$ in eq. (4.5), with respect to the parameters [82].

For an optical-model fit to a single angular distribution, in which statistics dominates the experimental uncertainties (excluding an overall normalization uncertainty) and for which the model can be forced to describe the data, the parameter uncertainties can be reliably estimated from such parametric models, assuming that Q^2 has a χ^2 distribution. We have verified this by fitting single data sets of $\sigma(\theta)$ and $A_y(\theta)$ using MINOPT; it is also the experience of most users of optical-potential search codes.

When the optical model is used to fit several data sets simultaneously in global parametrizations such as CH89, several problems hinder the interpretation of uncertainties. The two main difficulties are that there are usually systematic data uncertainties not accounted for by the statistical uncertainties usually reported (sections 4.2, 4.3), and such global parametrizations cannot be expected to describe all the data accurately. Most experimenters report only the statistical uncertainties, because they attempt to minimize systematic uncertainties in their data. Nevertheless, since the elastic-scattering measurements are now usually made with high statistical precision, non-statistical uncertainties can become important, especially in the normalization of data (sections 3, 4.2, and 4.3). Omission of these effects from the uncertainties results in higher contributions to $Q^2(\text{global})$ in eq. (4.5) for some data than for others, so that $Q^2(\text{global})$ no longer has an analytic, statistically straightforward interpretation, since it does not have a χ^2 distribution, as discussed in section 4.3.

Beyond such problems, which can be approximately corrected by the Q^2 renormalization described in section 4.3.2, the purpose of a global optical model is to describe, on the basis of well-justified physics (sections 1.4, 2.1), a large body of elastic-scattering data by a relatively small number of parameters. (In our analysis about 9000 data are described by 20 parameters.) The parameters are assumed to vary smoothly with Z , N , projectile type (p or n) and energy E , yet it is clear that the data contain local effects of shell structure and collectivity, which cannot be described in any simple systematic way within this model. The inability of the global optical model to describe local variations in elastic scattering contributes to the least-squares minimization of a non-statistical way.

However, it is still very useful to estimate uncertainties in the potential parameters. One might ask, ‘‘How different would the parameters of the global model be if another researcher with a similarly extensive, but different, database were to use a similar parametrization?’’ In the initial global

optical-model analysis, CH86 [13, 14], different methods of estimating uncertainties using MINUIT produced contradictory results. Eventually, without assuming that the search process gives accurate variances, or that the probability content of the Q^2 statistic is reliable, we found how to estimate parameter uncertainties and correlations reliably between parameters. This is the main difference between the CH86 and the present CH89 parametrizations.

5.2. The bootstrap uncertainty analysis

A recently invented technique for model-independent (non-parametric) statistical analysis is Efron's bootstrap [83, 84]. A pedagogical introduction to bootstraps is provided in a *Scientific American* article [85]. Originally, the bootstrap was used to estimate "standard errors" in simple statistical quantities, such as means and correlation coefficients, for data with unknown distributions. More recently, it has been used, for example, to analyze clustering of galaxies [86]. To our knowledge, this global optical-model analysis is the most complex uncertainty analysis to use the bootstrap technique.

The bootstrap simulates many repeated measurements of the data by creating new data sets of the same size as the original, using random sampling with replacement. That is, given a set of N data,

$$D = \{d_1, d_2, d_3, d_4, d_5, \dots, d_N\}, \quad (5.7)$$

and a quantity that depends on D , $X(D)$, we create K new data sets randomly. Thus, the j th one (D_j) may have, for example, d_1 appearing twice and d_5 deleted,

$$D_j^* = \{d_1, d_1, d_3, d_4, d_6, \dots\}, \quad (5.8)$$

and, correspondingly, $X_j = X(D_j^*)$. The distribution of the X_j indicates the likely spread of the X -values if the experiment were repeated K times. The width of this distribution is estimated by the standard deviation

$$\sigma(\bar{X}) = \left(\frac{1}{K-1} \sum_{j=1}^K (X_j - \bar{X})^2 \right)^{1/2}, \quad (5.9)$$

in which \bar{X} is the mean of the bootstrap samples X_j .

To obtain reliable parameter distributions in the application of the bootstrap to CH89, several hundred resamplings, K , were required. In our analysis each d_j is an angular distribution of $\sigma(\theta)$ and (usually) of $A_y(\theta)$ or $\sigma A_y(\theta)$. The X 's are optical-model parameters. Therefore, since the parameter search is computationally intensive, a bootstrap analysis for global optical-model parameters is time consuming and expensive.

5.3. A simple example of the bootstrap

As a straightforward example of the bootstrap applied to estimating parameter confidence intervals, consider a linear relation between two parameters but with superimposed random fluctuations. The parameters are intercept and slope, with their uncertainties, and a coefficient of correlation between them. In this example the uncertainties and correlation can also be estimated analytically from the

method of least squares, providing a check on the bootstrap. Using the bootstrapped data we can also demonstrate some properties and applications of the correlations.

The model function we choose is $y = x$ so that the intercept $b = 0$ and the slope $m = 1$. From this model we generate $N = 100$ synthetic data points, y , for $x = 1, 2, \dots, 100$. Analogously to our studies using synthetic optical-model data (section 4.2), we simulate uncertainties in the data by adding to each y a random number, chosen from a normal distribution with mean zero and standard deviation $\sigma(y) = 5$. These data and the least-squares best-fit line are shown in fig. 12a. The line, with its analytically estimated standard deviations, is

$$y = (1.2 \pm 1.0) + (0.98 \pm 0.02)x .$$

The analytically estimated correlation coefficient, $\rho(b, m) = -0.9$, indicating that small increases in b can be almost completely compensated by a decrease in m , as is evident from geometry.

For bootstrap estimates of parameter uncertainties, we select $K = 100$ bootstrap samples of the original data. Each sample has $N = 100$ data points, and a least-squares fit is performed for each sample. The distributions of b and m around their respective means, b_0 and m_0 , shown in figs. 12b and

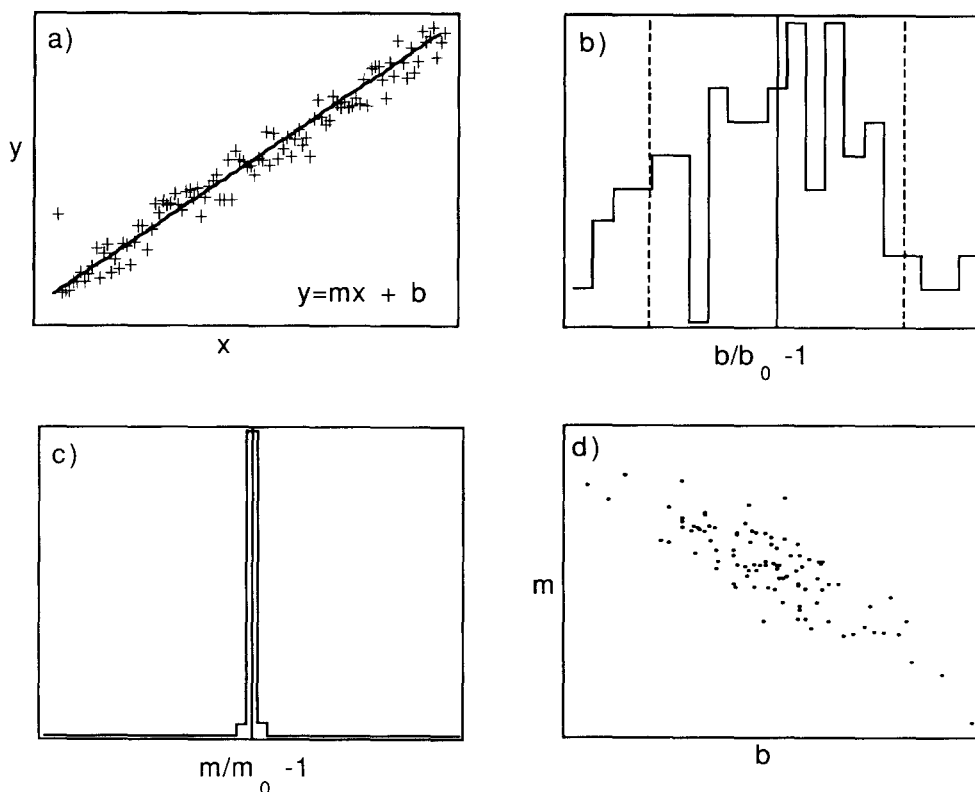


Fig. 12. Results of the simple bootstrap example with noisy, linear data: (a) the straight-line data points, shown with the least-squares best-fit line; (b) the bootstrap distribution of the intercept, b , scaled to contain values of b within 100% of the bootstrap mean, b_0 ; (c) the bootstrap distribution of the slope, m , scaled as b , relative to the mean slope, m_0 ; (d) a scatter plot of m against b , to display correlation in the determinations of the coefficients. The correlation coefficient of m and b is determined from the data in the scatter plot to be $\rho(m, b) \approx -0.8$.

12c are used to estimate the parameter standard deviations, $\Delta b = 1.0$ and $\Delta m = 0.02$, in agreement with the analytical result above. The correlation coefficient from the bootstrap data, using eq. (5.2), is $\rho(b, m) = -0.8$ for the scatter plot shown in fig. 12d. Thus, in this simple example the bootstrap essentially agrees with the analytic results because of the linearity of the model, but with a 100 times greater computational effort.

5.4. Bootstrapping for optical-potential uncertainties

For the CH89 optical-model analysis we extended the bootstrap technique to address the problem of parameter uncertainties by taking the original database (section 3) and selecting data sets repeatedly with replacement to construct new databases, each with the same number of data sets as the original, as in eq. (5.8). For each new database, we estimated, using MINOPT (section 4.1), the best set of parameter values for a global fit. The distributions of these parameters are shown in fig. 13.

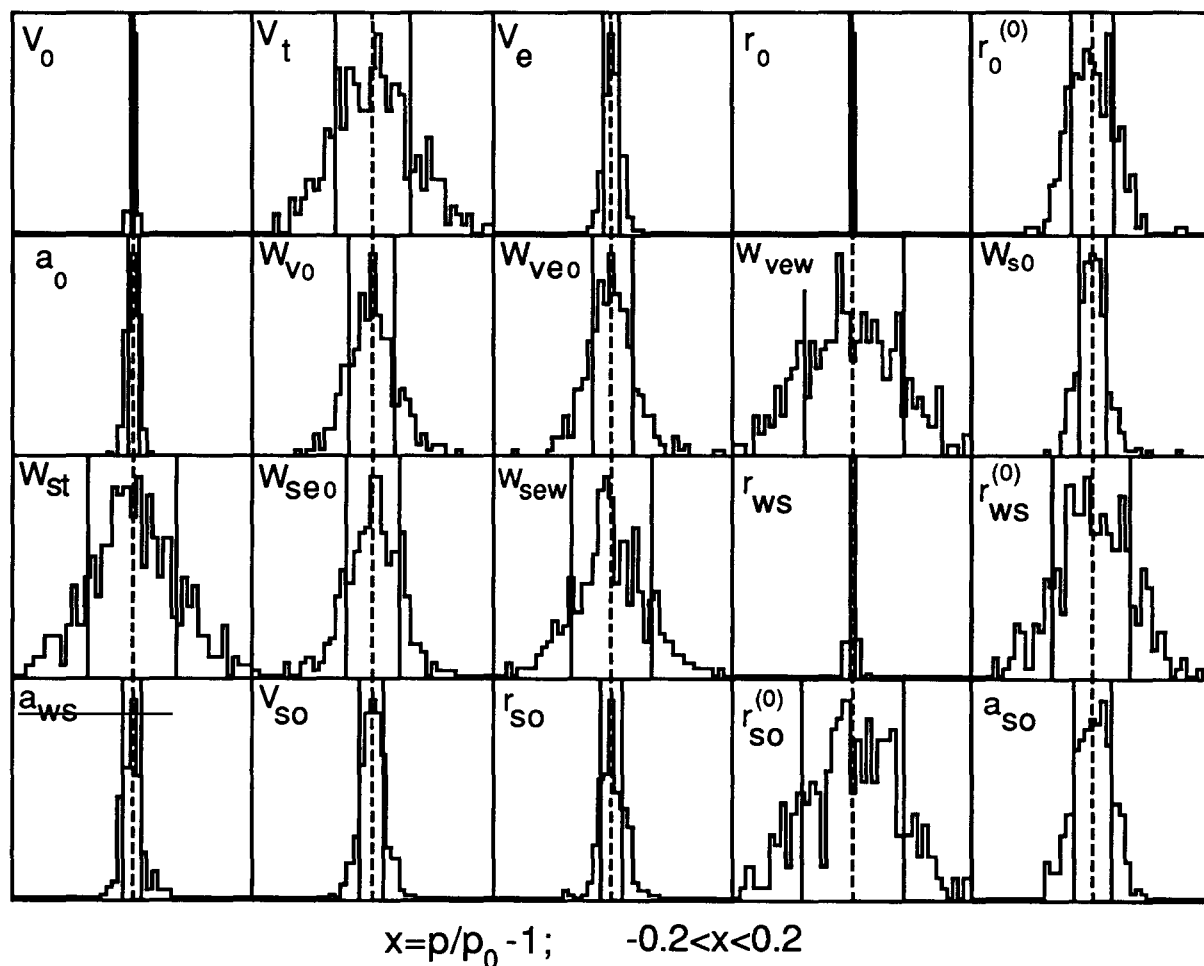


Fig. 13. Bootstrap distributions of the CH89 optical-model parameters. The horizontal axes show $x = p/p_0 - 1$, where p_0 is the mean value of the parameter in the bootstrap distribution. They are scaled to show x -values within the interval $[-0.2, 0.2]$. The point $x = 0$ is shown by the dashed line. The solid lines show the standard error interval. The bootstrap was performed with 300 samples of the 300 angular-distribution database.

Given the empirical parameter distributions from the bootstrap calculations, we then estimated the uncertainties of each global optical-model parameter as the half-width of the interval containing 68% of the probability of the distribution, centered symmetrically about the mean value of the parameter. Figure 13 shows that most parameter distributions are sufficiently symmetric for this purpose. We also estimated the correlation coefficients of the global parameters, using eq. (5.2), with x and y representing pairs of parameters.

The bootstrap estimates of uncertainties were found to be sufficiently accurate and stable for $K \leq 300$ samples, which is consistent with results in simpler systems [84]. It appears that the estimates of correlations are less accurate for this sample size, but they are sufficient for qualitative work. For a 300-sample estimate, the required CPU time on a modern scalar processor was about 150 h. Thus, the time per global search was about 30 min, rather than the 1 h cited in section 1.4.3, because each search started fairly near a minimum and refined convergence to a best fit was not required.

In order to test for systematic errors in estimating the uncertainties, we ran two test cases using different starting values of the potential parameters in the search. The searches resulted in similar

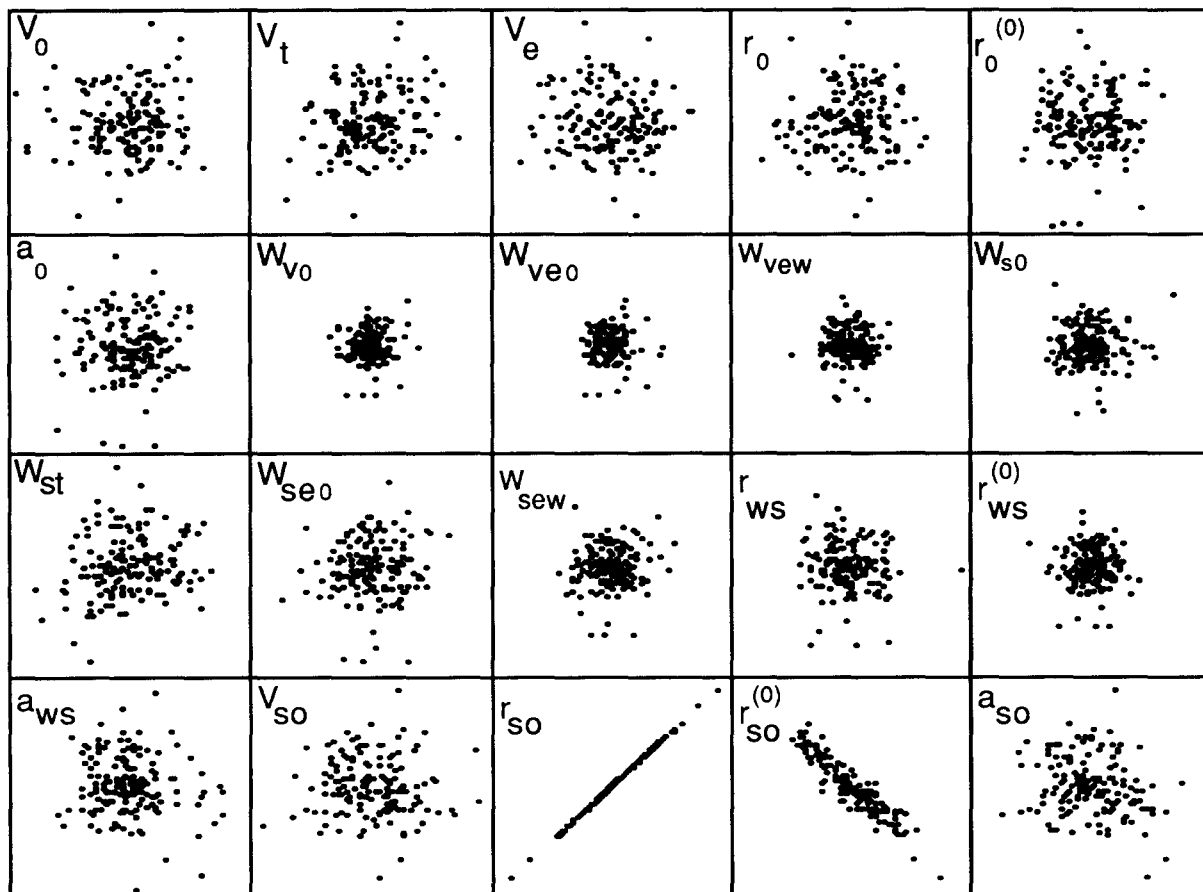


Fig. 14. Scatter plots of correlated parameters. The figure shows the correlation of r_{so} with all the other parameters in a bootstrap data set of 300 samplings of the global database. The axes are scaled so that the correlation ellipses would be aligned along a 45° line if the relative uncertainties in each pair of parameters were correctly estimated, as shown for the self-correlation of r_{so} .

distributions of the parameters and only slight differences in the final uncertainty estimates. The results of the bootstrap analyses are given in tables 6 and 7, while figs. 13 and 14 show the results visually.

6. The global optical potential, conclusions and outlook

In this section we reward the diligent reader by presenting the global potential parameters resulting from our investigation, their uncertainties, comparisons with previous work, some applications, and suggestions for further research. The potential parameters obtained in the final searches are those in table 6 and fits to the data are displayed in figs. 3 to 11 for representative values of A , Z , and E . Our estimates of the parameter confidence limits are in table 6 and the correlation coefficients are in table 7. We also discuss qualitatively the fits, then compare the volume integrals from the present potential with previous empirical parametrizations, with microscopically derived potentials, and with phenomenological values obtained from the literature.

6.1. The optical-model potential CH89

The features of this global optical-model potential were summarized in section 1.2. We now make some general observations and comparisons with previous nucleon–nucleus potentials.

6.1.1. Parameter values

The final parameters of our semiempirical optical potential are listed in table 6 in terms of the parameter definitions in table 3. The least well-determined parameters are those for (i) the energy dependence of the absorptive potential (W_{ve0} , W_{vew} , W_{se0} and W_{sew}), (ii) the radius parameters of the spin–orbit potential (r_{so} and $r_{so}^{(0)}$) and (iii) the isovector components of both the real and absorptive potentials (V_t and W_{st}). The difficulty with (i) is partially a consequence of the irregular distribution of the data in energy. Comparison of the energy dependence of the absorptive potential (fig. 1) with the distribution of the data (fig. 2) shows that the variation of W_s and W_v with energy is greatest where there is the least data, around 30 to 40 MeV. The spin–orbit radius parameters are highly correlated, as discussed in section 6.2.1. The isovector components of the potentials, although relatively poorly determined, have uncertainties consistent with those in the other depth parameters.

We investigated the optimal values of the Coulomb correction attenuation factor, α , in eq. (2.15). This factor might not be unity, as usually implied, if the interaction were localized in some region of r -space, such as the surface, and not distributed uniformly throughout the nucleus. Searches on α generally returned to the value $\alpha = 1.0$, with large uncertainties, so we fixed it at this value. In addition, we investigated the effect of switching on and off the absorptive potential Coulomb correction [48] and found no effect on the quality of fit. This is because the important quantity in these fits is the total volume integral, which is relatively constant in E . A shift applied equally to W_s and W_v does not affect that total.

6.1.2. Representative fits to angular distributions

In figs. 3 to 11 we display representative fits (broadly distributed in A and E) of the global potential to the database described in section 3. About 40% of the data are shown, with the full set of fits to essentially the same potential, CH86, being given in ref. [14]. Overall, the fits are excellent and are significantly better than those obtained by Becchetti and Greenlees [1] who described much less data.

More quantitatively, calculations using their potential (table 1) gave Q^2 [eq. (4.2)] values greater by a factor of three than calculations using CH89. A more detailed comparison of the potentials is made in section 6.3.1.

For targets with $40 \leq A \leq 70$ we describe the proton scattering data at energies below 65 MeV less well than does ref. [1]. The most poorly described targets were ^{40}Ca , $^{54,56}\text{Fe}$, and the isotopes of Ni. These data were not well described even by local optical-model fits, so the poor visual quality of the global fit is not surprising. In the case of neutron scattering, the lower- A data are poorly described at the low energies of 10, 11, and (to a lesser extent) 14 MeV, perhaps because of compound-nucleus effects. In proton scattering from the same targets, the backward-angle cross sections are typically underestimated. The Becchetti–Greenlees potential [1] generally describes the $A < 70$ data better than CH89, because they were biased by data-set selection to emphasize fitting light, closed-shell nuclei at low energies.

For targets of $A > 70$, the data are well described by CH89 at all energies for both neutron and proton scattering. There are a few exceptions to this observation: $^{90}\text{Zr}(p, p)$ at 16 MeV and $^{92,96,98,100}\text{Mo}(n, n)$ at 20 MeV. The Zr scattering is significantly underestimated compared to fits on nearby nuclei at the same energies, although a very good local fit to these data is possible. The Mo neutron scattering is overestimated by the calculations, again in contrast to nearby nuclei and in spite of the high-quality local fits to the data. We have no explanation for these exceptions.

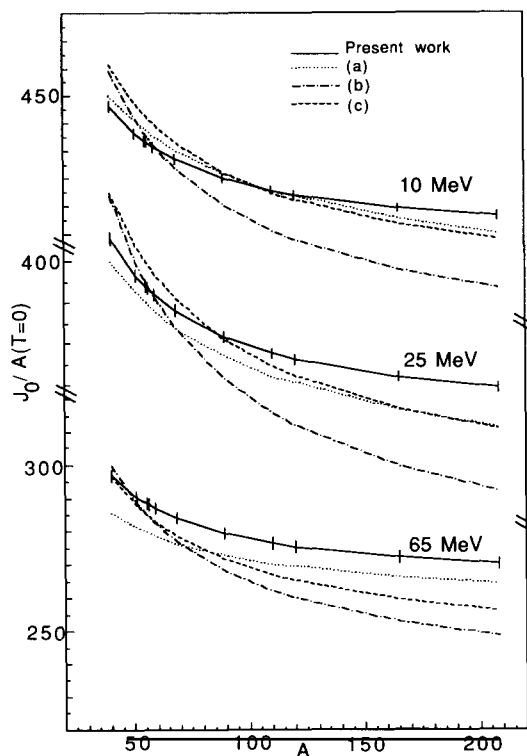


Fig. 15. Volume integrals of the real isoscalar central potential for CH89 and several other parametrizations. The other curves were constructed using the potentials from (a) Jeukenne et al. [3], (b) Becchetti and Greenlees [1], and (c) Rapaport [8]. The calculations were made at the three nucleon incident energies shown, for the 11 nuclei described in the text.

6.1.3. Volume integrals and RMS radii

To further characterize the CH89 potential, we present in figs. 15 to 18 the volume integrals and in fig. 19 the root-mean-square (RMS) radii of the CH89 potential in comparison with those of other global potentials [1, 3, 8]. The calculations were made for the same nuclei used in the folding-model calculations (section 2.1), ^{40}Ca , ^{51}V , ^{55}Mn , ^{56}Fe , ^{59}Co , ^{60}Ni , ^{65}Cu , ^{68}Zn , ^{89}Y , ^{110}Cd , ^{120}Sn , ^{165}Ho , and ^{208}Pb , for which 2pF nuclear charge densities are available [37, 38]. The calculations were made for $E = 10, 25,$ and 65 MeV. The volume integrals are shown separated into the $T = 0$ (isoscalar) and $T = 1$ (isovector) components and, for consistency, exclude Coulomb corrections. The comparison of volume integrals is developed in section 6.3.

6.1.4. Nuclear matter properties

To use CH89 as a test of nuclear-matter calculations and for use in neutron-star calculations, we write down the single-nucleon potential, with uncertainties, in the large- A limit for asymmetric matter, V_{nm} :

$$V_{\text{nm}} = -(52.9 \pm 0.2) \mp (13.1 \pm 0.8) \frac{N - Z}{A} + (0.299 + 0.004)E - i(7.8 \pm 0.3) \left[1 + \exp\left(\frac{(35 \pm 1) - E}{16 \pm 1}\right) \right]^{-1} \quad (6.1)$$

for $10 \leq E \leq 65$ MeV, where, in the isovector strength, the upper sign is for protons and the lower sign is

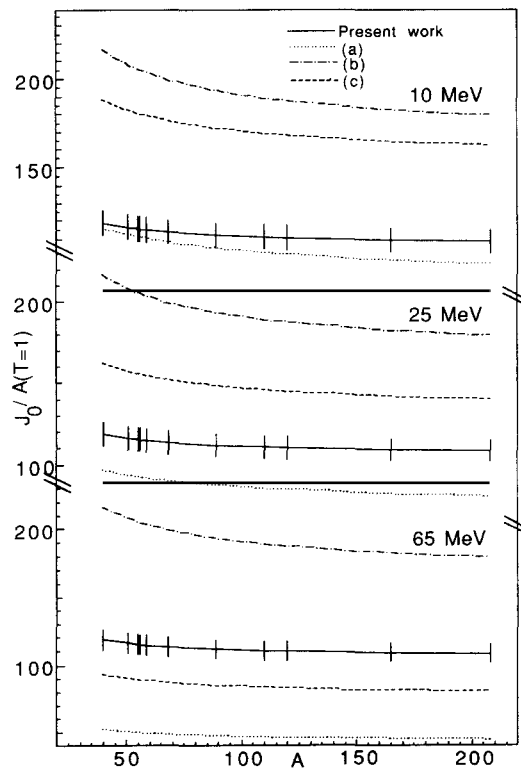


Fig. 16. Volume integrals for the real isovector central potential. See fig. 15 for details.

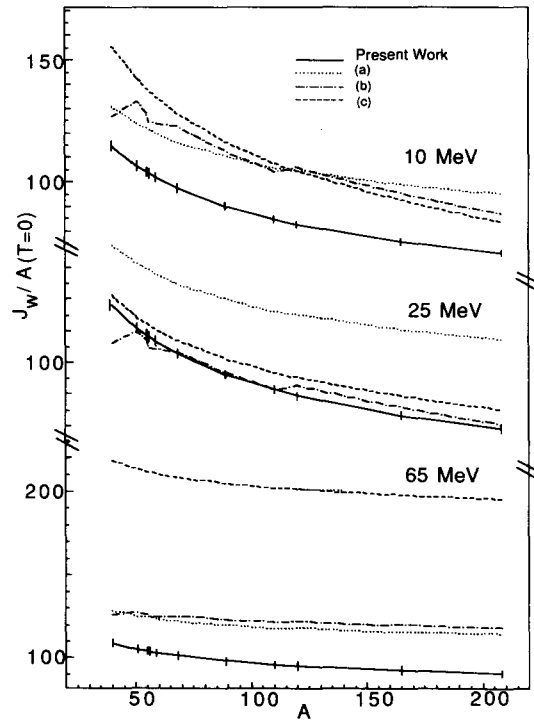


Fig. 17. Volume integrals for the absorptive isoscalar central potential. See fig. 15 for details.

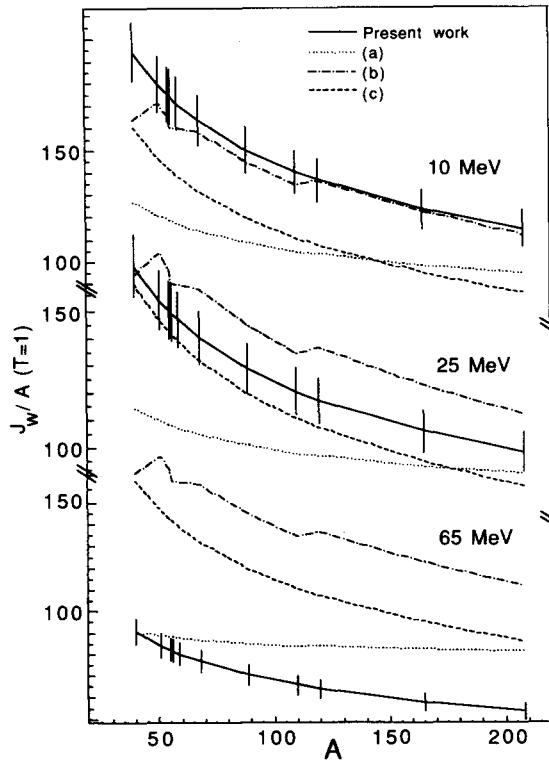


Fig. 18. Volume integrals for the absorptive isovector central potential. See fig. 15 for details.

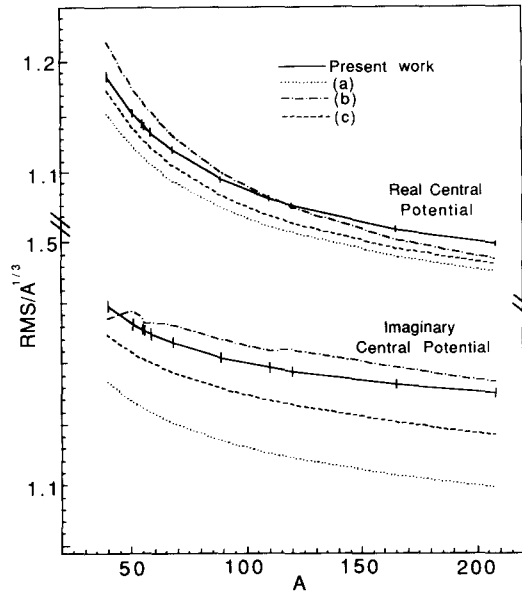


Fig. 19. RMS radii for the potentials shown in figs. 15 to 18. These calculations were made for nucleons of 25 MeV incident energy, which is irrelevant except for the calculations from ref. [3]. The radii are scaled by $A^{1/3}$.

for neutrons. In eq. (6.1) the appropriate energy for protons is not simply $E - E_c$, with E_c the Coulomb correction (section 2.4.2), but depends, for example, on how the momentum dependence is incorporated. In addition, there are correlations between the parameters in this equation, as discussed in section 6.2.

6.2. Parameter uncertainties, correlations and their uses

The parameter uncertainties and correlations were estimated using the bootstrap technique of Efron [83–85], as described in sections 5.2 to 5.4. They are listed in tables 6 and 7, and are displayed in figs. 13 and 14. To estimate these statistical quantities, we made about 300 bootstrap samplings and parameter optimizations, for a total of about 10^7 optical model calculations. We found it necessary to take great care when using the fitting program MINUIT (section 4.1) to reinitialize the covariance matrix between samplings, in order to be assured that the results of each sample were independent of previous resamplings.

6.2.1. Parameter uncertainties and their interpretation

In estimating the uncertainties of the optical-model parameters, we chose to use the “standard error” technique of Efron [87], in which we assume that the distribution of estimates from the bootstrap resamplings are sufficiently normal that the uncertainty can be estimated from the standard deviation. Inspection of the parameter distributions in fig. 13 justifies this assumption qualitatively. Thus, the uncertainties in table 6 are standard deviations of the bootstrap distribution for each parameter. The more sophisticated estimations of confidence intervals described in ref. [87] are not worthwhile because the model is limited in its ability to describe the data.

It is necessary to qualify the interpretation of the standard-error intervals that we report, as discussed in section 5.1. For normal distributions the meaning of the standard error, σ_i , for each parameter estimate, \bar{p}_i , is that there is a 68% chance that the true value of the parameter is in the interval $[\bar{p}_i - \sigma_i, \bar{p}_i + \sigma_i]$, but only if one ignores the simultaneous values of the other parameters. If we wish to make a statement about the simultaneous values of the parameters, we must use the bootstrap data set of parameters (300 sets of 20 optical-model parameters) as an approximation to the joint probability distribution of the parameters. From this we can determine intervals for all the parameters such that there is a 68% chance that all parameters are within these intervals. An approximation to this volume is the hyper-rectangle [80, ch. 9] for which,

$$P\left(\bigcap_{i=1}^n (\bar{p}_i - 2.2\sigma_i \leq p_i \leq \bar{p}_i + 2.2\sigma_i)\right) = 0.71, \quad (6.2)$$

where \cap designates the joint probability. Thus, there is a 71% probability that the true values of all the parameters are simultaneously within an interval of width 2.2 times the uncertainties we show in table 6, centered on the estimated parameter values.

Our bootstrap data set can be a powerful tool for studying a variety of statistics that summarize the parameters and their properties. We have exploited one possibility in the joint estimate presented in eq. (6.2). Another possibility is to estimate the uncertainties of functions of the parameters directly from the bootstrap data set. We do this by calculating the function for each of the bootstrap parameter sets, then measuring the uncertainty from the resulting distribution of function values. Such uncertainties will automatically include all correlations between parameters.

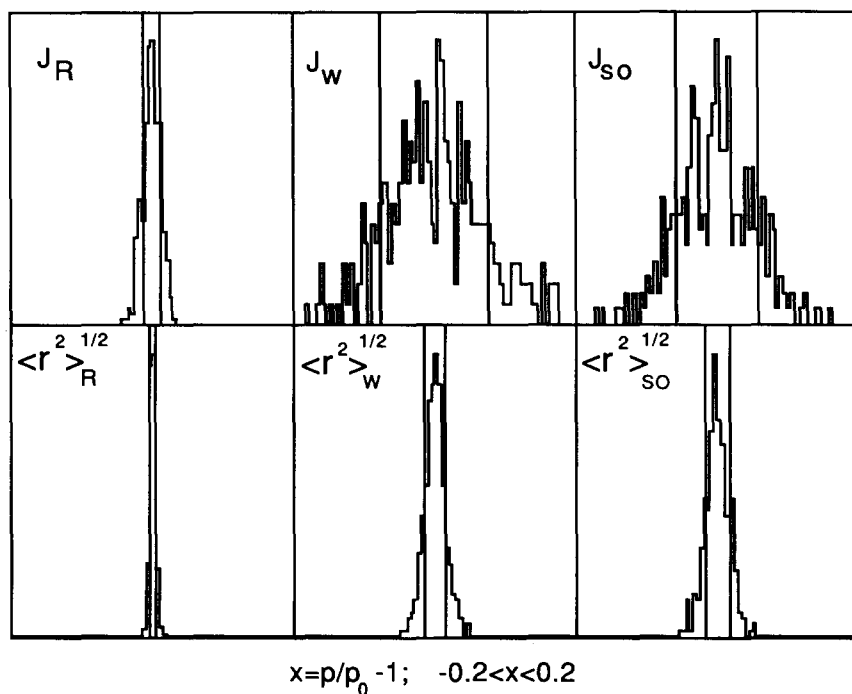


Fig. 20. Distribution of volume integrals and RMS radii calculated from the bootstrap samples. The horizontal axes are defined as in fig. 13. The standard errors of such distributions estimate the uncertainties shown in figs. 15 to 19. Mean values and standard deviations are given in eq. (6.3).

As an example, we estimate the uncertainties in the volume integrals and root-mean-square radii for the real central, imaginary central and spin-orbit potentials. The distributions calculated for $A = 125$, $Z = 50$ and $E = 30$ MeV neutron scattering are presented in fig. 20. The values and their standard deviations are,

$$\begin{aligned} J_{\text{R}} &= 341 \pm 2 \text{ MeV fm}^3, & \langle r^2 \rangle_{\text{R}}^{1/2} &= 5.33 \pm 0.01 \text{ fm}, \\ J_{\text{w}} &= 71 \pm 2 \text{ MeV fm}^3, & \langle r^2 \rangle_{\text{w}}^{1/2} &= 6.18 \pm 0.05 \text{ fm}, \\ J_{\text{so}} &= 222 \pm 7 \text{ MeV fm}^5, & \langle r^2 \rangle_{\text{so}}^{1/2} &= 5.54 \pm 0.05 \text{ fm}. \end{aligned} \tag{6.3}$$

A more concise method is to use the parameter values, uncertainties and correlation coefficients in tables 6 and 7, as we illustrate in section 6.2.3. Before doing this, we discuss the correlation coefficients between parameters in CH89.

6.2.2. Correlation matrix and its interpretation

Another useful statistic to estimate from the bootstrap data set of optical-model parameters is the pairwise correlation coefficient, described in section 5.1.1. The correlations, often written in a matrix, show whether the global optical-model parameters in CH89 are strongly interdependent, and allow estimates of the uncertainties for functions of the parameters.

We used the bootstrap analysis described in section 5.4 to estimate the correlation matrix presented in table 7. It is not as well determined as the standard deviations. In several different bootstrap calculations, using different starting potentials for each search on a bootstrap sample, our estimates of the correlations varied by ± 0.2 and we calculated the standard deviation of the bootstrap correlations to be ± 0.1 . Estimating these “higher-order” statistics from a bootstrap data set requires more care and more bootstrap samples than for simple standard deviations, as discussed in ref. [87]. For our purposes, the less precise correlation matrix is sufficient, but to emphasize this imprecision, we have eliminated all the elements from the correlation matrix with $|\rho| < 0.2$. In practice, such elements do not contribute much to the calculated uncertainties, in spite of the warnings in section 5.1.1.

The qualitative observation of correlation coefficients in the matrix in table 7 shows only three with $|\rho| \geq 0.5$. In particular, the correlation of r_{so} and $r_{\text{so}}^{(0)}$ is -1.0 , which means that r_{so} and $r_{\text{so}}^{(0)}$ cannot be determined independently within the uncertainties we measure. Another large correlation is between V_{so} and a_{so} ($\rho = 0.7$), suggesting a reciprocal relationship between the two parameters. Since V_{so} is a surface-peaked potential, the potential conserves a different property of the spin-orbit potential than the J_2 integral in eq. (1.6), perhaps its surface strength, which varies as $V_{\text{so}}/a_{\text{so}}$.

A large correlation between the absorption parameters W_{v0} and W_{ve0} ($\rho = 0.6$) is also indicated. Such a large correlation did not arise in all the bootstrap samples and so may be spurious. The reason for this relationship is not clear.

The well known and physically understood strong anticorrelations ($\rho \approx -1$) between the central-well depth, V_0 , and its radii, r_0 and $r_0^{(0)}$, for single angular distributions is weakened in a global database [$\rho(V_0, r_0) = -0.4$, $\rho(V_0, r_0^{(0)}) = -0.5$], presumably because of the large variation of nuclear radii over $40 \leq A \leq 209$. Thus the well depths V_0 and the radii r_0 and $r_0^{(0)}$ are determined independently and without ambiguity.

6.2.3. Example: calculation of spin-orbit integrals

The use of correlations in computing uncertainties of functions of the optical-model parameters, such as volume integrals, follows straightforwardly from the application of eq. (5.3) and its extension to several parameters [80]. As an example we show the analytic calculation of the uncertainty of J_{so} , which was computed directly from the bootstrap sample in eq. (6.3). The expression for J_{so} is given in eq. (2.9), and its uncertainty may be estimated from a simple extension of eq. (5.3),

$$\begin{aligned}
\sigma^2(J_{so}) = & \left(\frac{\partial J_{so}}{\partial V_{so}} \right)^2 \sigma^2(V_{so}) + \left(\frac{\partial J_{so}}{\partial r_{so}} \right)^2 \sigma^2(r_{so}) + \left(\frac{\partial J_{so}}{\partial r_{so}^{(0)}} \right)^2 \sigma^2(r_{so}^{(0)}) + \left(\frac{\partial J_{so}}{\partial a_{so}} \right)^2 \sigma^2(a_{so}) \\
& + 2\rho(V_{so}, r_{so}) \frac{\partial J_{so}}{\partial V_{so}} \frac{\partial J_{so}}{\partial r_{so}} \sigma(V_{so})\sigma(r_{so}) + 2\rho(V_{so}, r_{so}^{(0)}) \frac{\partial J_{so}}{\partial V_{so}} \frac{\partial J_{so}}{\partial r_{so}^{(0)}} \sigma(V_{so})\sigma(r_{so}^{(0)}) \\
& + 2\rho(V_{so}, a_{so}) \frac{\partial J_{so}}{\partial V_{so}} \frac{\partial J_{so}}{\partial a_{so}} \sigma(V_{so})\sigma(a_{so}) + 2\rho(r_{so}, r_{so}^{(0)}) \frac{\partial J_{so}}{\partial r_{so}} \frac{\partial J_{so}}{\partial r_{so}^{(0)}} \sigma(r_{so})\sigma(r_{so}^{(0)}) \\
& + 2\rho(r_{so}, a_{so}) \frac{\partial J_{so}}{\partial r_{so}} \frac{\partial J_{so}}{\partial a_{so}} \sigma(r_{so})\sigma(a_{so}) + 2\rho(r_{so}^{(0)}, a_{so}) \frac{\partial J_{so}}{\partial r_{so}^{(0)}} \frac{\partial J_{so}}{\partial a_{so}} \sigma(r_{so}^{(0)})\sigma(a_{so}). \quad (6.4)
\end{aligned}$$

To evaluate this equation, we require the derivatives of the volume integral, the values and uncertainties of the parameters in table 6, and the correlations from table 7. The derivatives are, including an evaluation using the data from tables 6 and 7, and using $A = 125$, $Z = 50$ for $E = 30$ MeV neutron scattering,

$$\begin{aligned}
\frac{\partial J_{so}}{\partial V_{so}} &= \frac{8\pi}{A} R_{so} (R_{so}^2 + \pi^2 a_{so}^2) = 39, \\
\frac{\partial J_{so}}{\partial r_{so}} &= \frac{8\pi V_{so}}{A^{2/3}} (3R_{so}^2 + \pi^2 a_{so}^2) = 576, \\
\frac{\partial J_{so}}{\partial r_{so}^{(0)}} &= \frac{8\pi V_{so}}{A} (3R_{so}^2 + \pi^2 a_{so}^2) = 115, \\
\frac{\partial J_{so}}{\partial a_{so}} &= \frac{8\pi V_{so}}{A} (2\pi^2 a_{so} R_{so}) = 81.
\end{aligned} \quad (6.5)$$

Upon combining these derivatives with the σ - and ρ -values from tables 6 and 7, we obtain

$$\sigma(J_{so}) = [449 \text{ (uncorrelated terms)} - 411 \text{ (correlation corrections)}]^{1/2} = 6 \text{ MeV fm}^5, \quad (6.6)$$

in good agreement with the bootstrap estimate in eq. (6.3), $\sigma(J_{so}) = 7 \text{ MeV fm}^5$.

This example shows the need for including correlations when evaluating uncertainties of functions of optical-potential parameters, since here neglecting correlations would increase the estimate of $\sigma(J_{so})$ by more than a factor of three, as eq. (6.6) shows.

6.3. Comparison with previous global analyses

As examples of how the CH89 parametrization improves over other phenomenological potentials and to show its application as a test of the microscopic potentials, we compare it with previous global parametrizations [1, 8, 23] and with the microscopic calculation of Jeukenne et al. [3]. We do not try to make a comparison with the microscopic model of Brieva and Rook [47], since their effective interaction is not available in a form usable at these energies. The bases for our comparisons are the volume integral per nucleon and the RMS radii of the potentials, defined and discussed in section 2.2, and evaluated for CH89 in eq. (6.3).

The microscopic calculations we make follow ref. [3], incorporating the energy- and density-dependent potentials in the local-density approximation, and including finite-range corrections. The matter densities used were calculated from the 2pF (sections 2.1 and 6.1.3) charge distributions [14].

The uncertainty bars are shown on each of the CH89 curves in figs. 15 to 19. These uncertainties were calculated from the same bootstrap data set as the volume integrals in eq. (6.3). As can be seen, none of the other models are consistently within our uncertainties over all target masses or energies. Clearly, the RMS radii are the best determined, and the isovector volume integrals are the least well determined. We now follow with detailed comparisons.

6.3.1. Real central potential

The comparisons of our real central-potential volume integrals with those of other phenomenological and microscopic potentials are shown in figs. 15 and 16, and the RMS radii are shown in fig. 19. Our isoscalar potential agrees relatively well with the others at low A , but we disagree at high A , where those from CH89 have more strength, especially compared with the Becchetti–Greenlees result. The energy dependence from CH89 is comparable to that from the other potentials.

In the comparison of the isovector volume integrals the discrepancies are more striking. It is clear that the Becchetti–Greenlees [1] value for the isovector volume integral is much too large at most energies. The Rapaport potential [8] agrees best at the highest energies, and the model of Jeukenne et al. [3] agrees best at the lowest energies. Certainly, one sees that lower isovector strengths than are typically used in optical-model calculations are preferred by our analysis.

To test the consistency of CH89 with optical-model analyses at higher energies, we calculated J_v for ^{90}Zr at $E = 65$ MeV from the (p, p) results of Nadasen et al. [18], the “fixed spin–orbit result”, for which $J_v/A = 329 \pm 10$ MeV fm³. For CH89 at this energy we obtain very good agreement, $J_v/A \approx 323 \pm 2$ MeV fm³, with the calculations using the Coulomb-corrected proton energy.

6.3.2. Spin–orbit potential

Because V_{so} is independent of energy in CH89, comparison of spin–orbit volume integrals of empirical optical-model potentials should be straightforward. However, the only microscopic calculation of the spin–orbit potential with which to compare is that of Brieva and Rook [14], which calculates the integral,

$$K_R = 8\pi V_{so} R_{so} A^{-1/3}. \quad (6.7)$$

Their model result is $K_R = 102$ MeV fm³, independent of A . However, for the CH89 potential, values of K_R range from 146 ± 2 MeV fm³ ($A = 40$) to 171 ± 3 MeV fm³ ($A = 208$), consistent with the Becchetti–Greenlees potential $K_R = 157$ MeV fm³.

The discrepancies between the empirical and the Brieva–Rook model results are large. However,

folding-model calculations of the spin-orbit potential [36] using M3Y effective interactions [40] obtain $K_R = 150 \text{ MeV fm}^3$, which is in good agreement with our results. The folding-model calculations also agree with our result that the E - and A -dependences of the spin-orbit potential are small. The CH89 depths and geometric parameters are consistent with previous analyses of spin-orbit coupling in bound and scattering states [31, 32], which show

$$V_{so} = (6.0 \pm 0.5) - (0.023 \pm 0.012)E \text{ MeV fm}^2, \quad r_{so} \approx 1.1 \text{ fm}, \quad a_{so} \approx 0.62 \text{ fm},$$

for $-20 \leq E \leq 200 \text{ MeV}$, with no A or isospin dependence.

We also investigated imaginary components of the spin-orbit potential. The value found for this term was less than 1 MeV, with an estimated uncertainty much larger than 1 MeV. Thus, from the CH89 analysis of our extensive database, there is no evidence for an imaginary component of the spin-orbit potential in a global optical-model potential.

6.3.3. Absorptive central potential

The volume integrals of the imaginary potential are shown in figs. 17 and 18, and the RMS radii are shown in fig. 19. The uncertainties shown with the CH89 calculations were calculated in the same manner as for the real potential. At most E - and A -values the potentials calculated from the other models are outside the uncertainty of our potential. At 25 MeV the empirical potentials are relatively close together, but by 65 MeV the model of ref. [8] is outside its reasonable limits of application, and so has too much absorption because of the linear-energy dependence. A similar problem would occur for the Becchetti-Greenlees potential [1] at any energy above 65 MeV.

The isovector volume integral, fig. 18, is somewhat misleading at 65 MeV, since the surface absorption cut-off (section 1) for the potentials of refs. [1] and [8] is slightly below this energy. In these potentials, the isovector component of the absorption is only in the surface term and is zero when the surface absorption is zero. However, the isovector contribution is independent of energy up to this cut-off, and so is shown as such in fig. 18.

Figure 1 displays the (p, p) absorption volume integrals for $A = 125$, $Z = 50$, and shows that CH89 is consistent with the phenomenological observation of ref. [17], $J_w/A = 115 \text{ MeV fm}^3$ for (p, p) scattering for $10 \leq E \leq 200 \text{ MeV}$. CH89 typically has a 3% uncertainty for the absorptive volume integral. Over a limited energy range, the potentials of refs. [1] and [8] are consistent with the phenomenology of ref. [17]. Above $E = 55 \text{ MeV}$, however, only CH89 maintains this consistency.

We compared our parametrization of the imaginary potential with the (p, p) analysis of Nadasen et al. [18], again for ^{90}Zr at $E_p = 65 \text{ MeV}$, which found a constant value of the volume integral of $J_w/A = 98 \pm 10 \text{ MeV fm}^3$, consistent with our estimate of $J_w/A \approx 110 \pm 2 \text{ MeV fm}^3$.

6.4. Outlook

We discuss here the directions that further research utilizing and improving optical-model potentials, such as CH89, may take. First, we summarize the unique features of this potential.

6.4.1. Features of CH89

The notable features of the CH89 potential are described in section 1.2. They include:

- (i) derivation from a much more extensive database of elastic scattering than previously used;
- (ii) a much weaker real central isovector potential than reported in previous global analyses;

- (iii) radius parameters that are A -dependent for all the potential parameters;
- (iv) a smooth variation in the absorptive potential with incident energy, allowing smooth extrapolation of the potential to higher energies and without discontinuities in the slope of the potential;
- (v) a spin-orbit potential depth independent of A and E , based on the inclusion of many more analyzing-power data than in any previous global analysis;
- (vi) parameter uncertainties and correlations, a feature missing from all previous global analyses.

In any such global analysis, major compromises must be made to summarize the result in a usable form. The compromise is in the quality of the fit, which, while good for so few parameters (20 parameters for 9000 data), could probably be improved by removing some constraints on the form of the potential. We describe below some of the possible directions for such research.

6.4.2. *Local fits compared with global fits*

The relatively poor fits to some data sets suggests a fruitful direction for future research, that of comparing the parameters of detailed fits to individual nuclei with the global parameters, in order to study nuclear-structure effects. If coupled-channel calculations were performed on the same scale as this research, about two orders of magnitude greater computation power than available for this work would be required.

6.4.3. *Data resources required*

Complementary (p, n) data required for a complete description of the isovector potential are desirable, as well as elastic (n, n) data at energies above 30 MeV. Such data would have to be precise and relatively extensive to influence the large database of elastic scattering we have already assembled. The parametrization of the energy dependence of the imaginary potential and of the spin-orbit potential would be helped by the inclusion of new data in the energy region of 30 to 60 MeV. These new measurements should include analyzing powers as well as cross sections.

6.4.4. *Other descriptions of the optical potential*

We have constrained the CH89 optical-model potential to resemble the optical model used in previous global analyses such as those given in refs. [1] and [8]. While such a representation has been successful in fitting data, and is not inconsistent with theoretical expectations (section 2), it would be worthwhile to extend the form of the optical potential in order to try for more uniformly good fits to the elastic scattering data. Such extensions might include more general form factors, for example, three-parameter Fermi or Fourier-Bessel expansions, and a more general representation of the isovector interaction in terms of the difference between the neutron and proton densities in a folding-model approach.

It should also be possible to take this analysis one level deeper in the optical potential, to parametrize the effective interaction, as was attempted earlier [26, 39]. With much faster computation, a more complete database, and improved understanding of the effective nucleon-nucleon interaction now available, such a project becomes feasible. Use of exact densities would help to remove one significant uncertainty of the optical potential, that of geometric parameters, which tend to be correlated with depth parameters. Such analyses may challenge the brave (and tempt the foolhardy) among nuclear phenomenologists.

Acknowledgements

The authors wish to acknowledge the generous assistance of many people in various aspects of this work. Many of the data we used were measured by other groups. We acknowledge especially Dr P.J. van Hall, who provided pre-publication tables of the Eindhoven data, and Dr H. Sakaguchi, who provided tables of the Osaka data. In addition, we thank members of the TUNL neutron scattering group, Drs R.L. Walter, R.S. Pedroni, C.E. Floyd, G. Honore, and P.P. Guss for tables of data and many discussions about the difficulties of neutron elastic scattering and the neutron optical model. The (p, p) data were measured at TUNL with the assistance of Drs D. Abbott, J. Bowsher, R.E. Fauber, B.C. Karp, T.M. Mooney, and T. Spencer. One of us (RLV) particularly wishes to acknowledge the invaluable assistance and advice of Drs. R.E. Anderson, B.L. Burks and J.F. Wilkerson in the course of this work, as well as the extensive help of D. Levine in development of the optical model program.

References

- [1] F.D. Becchetti and G.W. Greenlees, *Phys. Rev.* 182 (1969) 1190.
- [2] J.-P. Jeukenne, A. Lejeune and C. Mahaux, *Phys. Rep.* 25 (1976) 83.
- [3] J.-P. Jeukenne, A. Lejeune and C. Mahaux, *Phys. Rev. C* 15 (1977) 10; *C* 16 (1977) 80.
- [4] R. Machleidt, K. Holinde and Ch. Elster, *Phys. Rep.* 149 (1987) 1.
- [5] H. Feshbach, *Ann. Rev. Nucl. Sci.* 8 (1958) 49.
- [6] P.E. Hodgson, *Nuclear Reactions and Nuclear Structure* (Clarendon Press, Oxford, 1971).
- [7] G.R. Satchler, *Direct Nuclear Reactions* (Oxford, New York, 1983).
- [8] J. Rapaport, *Phys. Rep.* 87 (1982) 25.
- [9] J. Rapaport, R.W. Finlay, S.M. Grimes and F.S. Dietrich, eds, *Neutron-Nucleus Collisions – a Probe of Nuclear Structure*, AIP Conf. Proc. 124 (AIP, New York, 1985).
- [10] W.J. Thompson, T.L. McAbee and R.L. Varner, *Phys. Lett. B* 182 (1986) 247.
- [11] J.W. Truran, *Annu. Rev. Nucl. Part. Sci.* 34 (1984) 53.
- [12] E.T. Chang, *Fusion Technol.* 8 (1985) 1423.
- [13] R.L. Varner, T.B. Clegg, T.L. McAbee and W.J. Thompson, *Phys. Lett. B* 185 (1987) 6.
- [14] R.L. Varner, Ph.D. Dissertation (Univ. of North Carolina, 1986) unpublished (available from University Microfilms, Ann Arbor, MI, 48106).
- [15] W.D. Myers, *Nucl. Phys. A* 204 (1973) 465.
- [16] P.E. Hodgson, *Rep. Prog. Phys.* 47 (1984) 613.
- [17] D.C. Agrawal and P.C. Sood, *Phys. Rev. C* 11 (1975) 1854;
P.E. Hodgson, *Phys. Lett. B* 65 (1976) 331;
S. Kailas and S.K. Gupta, *Phys. Lett. B* 71 (1977) 271.
- [18] A.D. Nadasen, P. Schwandt, P.P. Singh, W.W. Jacobs, A.D. Bacher, P.T. Debevec, M.D. Kaitchuk and J.T. Meek, *Phys. Rev. C* 23 (1981) 1023.
- [19] C. Mahaux and R. Sartor, *Phys. Rev. Lett.* 57 (1986) 3015.
- [20] C.J. Batty, E. Friedman, H.J. Gils and H. Rebel, in: *Advances in Nuclear Physics*, vol. 19, eds J.W. Negele and E. Vogt (Plenum, New York, 1989) p. 1.
- [21] B.C. Clark, S. Hama, S.G. Kalbermann, E.D. Cooper and R.L. Mercer, in: *Neutron-Nucleus Collisions – a Probe of Nuclear Structure*, eds J. Rapaport, R.W. Finlay, S.M. Grimes and F.S. Dietrich, AIP Conf. Proc. 124 (AIP, New York, 1985) p. 123.
- [22] F.G. Perey, *Phys. Rev.* 131 (1963) 745.
- [23] J. Rapaport, V. Kulkarni and R.W. Finlay, *Nucl. Phys. A* 330 (1979) 15.
- [24] D.M. Patterson, R.R. Doering and A. Galonsky, *Nucl. Phys. A* 263 (1976) 261.
- [25] H.V. von Geramb, ed., *Microscopic Optical Potentials* (Springer, Berlin, 1979).
- [26] G.W. Greenlees, G.J. Pyle and Y.C. Tang, *Phys. Rev.* 171 (1968) 1115.
- [27] M.A. Preston and R.K. Bhaduri, *Structure of the Nucleus* (Addison-Wesley, Reading, MA, 1975).
- [28] G.W. Greenlees, W. Makofske and G.J. Pyle, *Phys. Rev. C* 1 (1970) 1145.
- [29] D.K. Srivastava, *Phys. Lett. B* 112 (1982) 289.
- [30] G.W. Greenlees, V. Hnizdo, O. Karban, J. Lowe and W. Makofske, *Phys. Rev. C* 2 (1970) 1063.
- [31] S.G. Cooper and P.E. Hodgson, *J. Phys. G* 6 (1980) L21.

- [32] J.A. Ramirez and W.J. Thompson, *J. Phys. G* 6 (1980) L113.
- [33] R.L. Walter, in: *Neutron–Nucleus Collisions – a Probe of Nuclear Structure*, eds J. Rapaport, R.W. Finlay, S.M. Grimes and F.S. Dietrich, AIP Conf. Proc. 124 (AIP, New York, 1985) p. 53.
- [34] F. James and M. Roos, *Comput. Phys. Commun.* 10 (1975) 343.
- [35] D.L. Smith, *Rev. Sci. Instrum.* 54 (1983) 818.
- [36] T.L. McAbee, Ph.D. dissertation (Univ. of North Carolina, 1986) unpublished (available from University Microfilms, Ann Arbor, MI, 48106).
- [37] C.W. de Jager, H. de Vries and C. de Vries, *At. Data Nucl. Data Tables* 14 (1974) 479.
- [38] H. de Vries, C.W. de Jager and C. de Vries, *At. Data Nucl. Data Tables* 36 (1987) 495.
- [39] A. Tarrats and J.L. Escudie, in: *Microscopic Optical Potentials*, ed. H.V. von Geramb (Springer, Berlin, 1979) p. 200.
- [40] G. Bertsch, J. Borysowicz, H. McManus and W.G. Love, *Nucl. Phys. A* 284 (1977) 399.
- [41] R.W. Haase and W.D. Myers, *Geometrical Relationships of Macroscopic Nuclear Physics* (Springer, Berlin, 1988).
- [42] A.M. Lane, *Rev. Mod. Phys.* 29 (1957) 191.
- [43] R. Hofstadter, *Rev. Mod. Phys.* 28 (1956) 214.
- [44] F. Osterfeld, *Phys. Rev. C* 24 (1981) 2408.
- [45] C. Mahaux and H. Ngo, *Phys. Lett. B* 126 (1983) 1.
- [46] J. Rapaport, *Phys. Lett. B* 92 (1980) 233.
- [47] F.A. Brieva and J.R. Rook, *Nucl. Phys. A* 291 (1977) 299; *A* 291 (1977) 317; *A* 297 (1977) 206; *A* 307 (1978) 493.
- [48] F. Osterfeld and V.A. Madsen, in: *Neutron–Nucleus Collisions – a Probe of Nuclear Structure*, eds J. Rapaport, R.W. Finlay, S.M. Grimes and F.S. Dietrich, AIP Conf. Proc. 124 (AIP, New York, 1985) p. 26.
- [49] A. Bohr and B.R. Mottelson, *Nuclear Structure*, vol. 1 (Benjamin, New York, 1969).
- [50] H.J. Yuan, H.L. Lin, G. Fai and S.A. Moszkowski, *Phys. Rev. C* 40 (1989) 1448.
- [51] J. Leeb and G. Eder, in: *Microscopic Optical Potentials*, ed. H. von Geramb (Springer, Berlin, 1979) p. 181.
- [52] G. Honore, private communication.
- [53] J.J.H. Menet, E.E. Gross, J.J. Malanify and A. Zucker, *Phys. Rev. C* 4 (1971) 1114.
- [54] S.D. Wassenaar, P.J. van Hall, S.S. Klein, G.J. Nijgh, J.H. Polane and O.J. Poppema, *J. Phys. G* 15 (1989) 181; S.D. Wassenaar, dissertation (Technische Hogeschool Eindhoven, 1982) unpublished.
- [55] J.P.M.G. Melssen, P.J. van Hall, S.D. Wassenaar, O.J. Poppema, G.J. Nijgh and S.S. Klein, *Nucl. Phys. A* 376 (1982) 183.
- [56] M.P. Fricke, E.E. Gross, B.J. Morton and A. Zucker, *Phys. Rev.* 156 (1967) 1207; L.N. Blumberg, E.E. Gross, A. van der Woude, A. Zucker and R.H. Bassel, *Phys. Rev.* 147 (1966) 812.
- [57] C.B. Fulmer, J.B. Ball, A. Scott and M.L. Whitten, *Phys. Rev.* 181 (1969) 1565.
- [58] H. Sakaguchi, M. Nakamura, K. Hatanaka, A. Goto, T. Noro, F. Ohtani, H. Sakamoto, H. Ogawa and S. Kobayashi, *Phys. Rev. C* 26 (1982) 944.
- [59] H. Sakaguchi, *Mem. Fac. Sci. Kyoto Univ. Ser. Phys. Astrophys. Geophys. Chem.* XXXVI (1982) no. 2, article 4.
- [60] C.E. Floyd, P.P. Guss, R.C. Byrd, K. Murphy, R.L. Walter and J.P. Delaroche, *Phys. Rev. C* 28 (1983) 1498; C.E. Floyd, dissertation (Duke Univ., 1981) unpublished.
- [61] S.M. El-Kadi, C.E. Nelson, F.O. Purser, R.L. Walter, A. Beyerle, C.R. Gould and L.W. Seagondollar, *Nucl. Phys. A* 390 (1982) 509.
- [62] P.P. Guss, R.C. Byrd, C.E. Floyd, C.R. Howell, K. Murphy, G. Tungate, R.S. Pedroni, R.L. Walter, J.P. Delaroche and T.B. Clegg, *Nucl. Phys. A* 438 (1985) 187; P.P. Guss, dissertation (Duke Univ., 1982) unpublished.
- [63] G. Honore, Ph.D. dissertation (Duke University, 1986) unpublished.
- [64] D.E. Bainum, R.W. Finlay, J. Rapaport, J.D. Carlson and W.G. Love, *Phys. Rev. C* 16 (1977) 1377; D.E. Bainum, R.W. Finlay, J. Rapaport, M.H. Hadizadeh and J.D. Carlson, *Nucl. Phys. A* 311 (1978) 492; J.C. Ferrer, J.D. Carlson and J. Rapaport, *Nucl. Phys. A* 275 (1977) 325; S. Mellema, R.W. Finlay, F.S. Dietrich and F. Petrovich, *Phys. Rev. C* 28 (1983) 2267; J. Rapaport, T.S. Cheema, D.E. Bainum, R.W. Finlay and J.D. Carlson, *Nucl. Phys. A* 296 (1978) 95; J. Rapaport, T.S. Cheema, D.E. Bainum, R.W. Finlay and J.D. Carlson, *Nucl. Phys. A* 313 (1979) 1; J. Rapaport, M. Mirzaa, H. Hadizadeh, D.E. Bainum and R.W. Finlay, *Nucl. Phys. A* 341 (1980) 56; Y. Yiming, C.E. Brient, R.W. Finlay, G. Randers-Pehrson, A. Marcinkowski, R.C. Taylor and J. Rapaport, *Nucl. Phys. A* 390 (1982) 449.
- [65] G. Ohlsen and P.W. Keaton Jr, *Nucl. Instrum. Meth.* 109 (1973) 41.
- [66] T.B. Clegg, G.A. Bissinger and T.A. Trainor, *Nucl. Instrum. Meth.* 120 (1974) 445.
- [67] B.L. Burks, Ph.D. dissertation (Univ. of North Carolina, 1983) unpublished (available from University Microfilms, Ann Arbor, MI, 48106).
- [68] G. Ohlsen, J.L. McKibben, G.P. Lawrence, P.W. Keaton Jr and D.D. Armstrong, *Phys. Rev. Lett.* 27 (1971) 599; P. Schwandt, T.B. Clegg and W. Haerberli, *Nucl. Phys. A* 163 (1971) 432; D.C. Dodder, G.M. Hale, Nelson Jarmie, J.H. Jett, P.W. Keaton Jr, R.A. Nisley and K. Witte, *Phys. Rev. C* 15 (1977) 518.
- [69] C.R. Gould and N.R. Roberson, *IEEE Trans. Nucl. Sci.* NS-30 (1983) 3758 and references therein.
- [70] W. Makofske, G.W. Greenlees, H.S. Liers and G.J. Pyle, *Phys. Rev. C* 5 (1972) 780.
- [71] R. Melzer, P. von Brentano, H. Paetz gen. Schieck, *Nucl. Phys. A* 432 (1985) 363.
- [72] W.T.H. van Oers, *Phys. Rev. C* 10 (1974) 307.

- [73] J.F. Dicello, G. Igo, W.T. Leland and F.G. Perey, *Phys. Rev. C* 4 (1971) 1130.
- [74] P.J. van Hall, private communication (1984).
- [75] P.J. van Hall, J.P.M.G. Melssen, S.D. Wassenaar, O.J. Poppema, S.S. Klein and G.J. Nijgh, *Nucl. Phys. A* 291 (1977) 63.
- [76] R.J. Eastgate, W.J. Thompson and R.A. Hardekopf, *Comput. Phys. Commun.* 5 (1973) 69.
- [77] W.J. Thompson, *Computing in Applied Science* (Wiley, New York, 1984) p. 152.
- [78] F. James, *Function Minimization*, in: *Proc. 1972 CERN Computing and Data Processing School*, CERN 72-21 (CERN, 1972).
- [79] R. Fletcher, *Comput. Phys. Commun.* 3 (1972) 159.
- [80] W.T. Eadie, E. Drijard, F.E. James, M. Roos and B. Sadoulet, *Statistical Methods in Experimental Physics* (North-Holland, Amsterdam, 1971).
- [81] J.R. Taylor, *An Introduction to Error Analysis* (University Science Books, Mill Valley, CA, 1982).
- [82] F. James, *Interpretation of the errors on parameters as given by MINUIT*, Supplement to CERN D-506 (1978) unpublished.
- [83] B. Efron, *Biometrika* 68 (1981) 589.
- [84] B. Efron, *SIAM Rev.* 21 (1979) 460.
- [85] P. Diaconis and B. Efron, *Sci. Am.* 248 (May, 1983) p. 116.
- [86] E.N. Ling, C.S. Frenk and J.D. Barrow, *Mon. Not. R. Astron. Soc.* 223 (1986) 21P.
- [87] B. Efron and R. Tibshirani, *Stat. Sci.* 1 (1986) 54.